Haris Naveed

Channel Modeling from FMCW Radar

School of Technology and Innovation

Master's Programme in Computing Sciences

Sustainable and Autonomous Systems

Vaasa 2025

Foreword

The research took place at the Center for Wireless Communications – Radio Technologies (CWC-RT) research unit within the University of Oulu Finland under Associate Professor Onel Luis Alcaraz López guidance. The work is part of my master's degree at the University of Vaasa under the supervision of Professor Mohammed Elmusrati.

I am deeply thankful to Associate Professor Onel Luis Alcaraz López for providing essential supervision, technical guidance and continuous support throughout the thesis process. I have enjoyed the privilege of working under him, while learning valuable lessons at the same time. I also want to thank Professor Mohammed Elmusrati for his academic oversight and feedback.

Finally, I want to express my appreciation to my family and friends for their love, prayers, and endless support throughout this entire process.

Oulu, May 15, 2025

Haris Naveed

UNIVERSITY OF VAASA
School of Technology and Innovations
Author: Haris Naveed
Thesis title: Channel Modeling from FMCW radar
Degree: Master of Science in Technology
Discipline: Sustainable and Autonomous Systems
Supervisor: Mohammed Elmusrati
Co-Supervisor: Onel Luis Alcaraz López
Year of graduation: 2025 **Number of pages:** 63

ABSTRACT:
An effective modeling of wireless communication channels is crucial for emerging technologies such as autonomous transportation and smart infrastructure, specially to ensure robust connectivity, optimize network performance, and enable adaptive communication under varying environmental conditions. In this thesis, a radar data-driven framework for wireless channel modeling using Frequency Modulated Continuous Wave (FMCW) radar, with a primary focus on path loss estimation in a Vehicle-to-Infrastructure (V2I) single-target scenario, is presented. The proposed methodology is based on signal processing techniques for range and velocity estimation for the detection and separation of target and stationary clutter in the V2I single-target scenario. Cell-Averaging Constant False Alarm Rate (CA-CFAR) is used to minimize the background and improve the detection of objects in the environment. Furthermore, the clustering is applied to organize clutter patterns and extract relevant features. From the processed data, path loss is calculated separately for both the moving object and the surrounding clutter. These path loss profiles are then fitted to empirical Alpha-Beta (AB) and Alpha-Beta-Gamma (ABG) models capturing overall propagation characteristics. The AB model demonstrates superior fitting performance. The proposed modeling framework characterizes the wireless environment effectively with the data available from radar. This provides systematic foundational methodology for future sensing-based propagation models, used in autonomous systems and smart infrastructure applications.

Keywords: FMCW Radar, Range-Doppler Processing, CA-CFAR, Clustering, V2I Communication, Path Loss, AB Model, ABG Model, Channel Modeling, Radar Sensing

Contents

List of Figures

List of Tables

Abbreviations

3GPP	3rd generation partnership project
AB	Alpha-beta (floating intercept) model
ABG	Alpha-beta-gamma model
ACC	Adaptive cruise control
ADC	Analog-to-Digital converter
ADAS	Advanced driver assistance systems
AEB	Automatic emergency braking
AoA	Angle of arrival
AR	Automotive radar
CA-CFAR	Cell-averaging constant false alarm rate
CUT	Cell under test
CW	Continuous wave
DSP	Digital signal processing
FMCW	Frequency modulated continuous wave
FDTD	Finite-difference time-domain
FMM	Fast multipole method
GMDM	Gaussian mixture density model
GO	Geometric optics
GPS	Global positioning system
IF	Intermediate frequency
IoT	Internet of things
LiDAR	Light detection and ranging
LNA	Low noise amplifier
MIMO	Multiple input multiple output
MoM	Method of moments
mmWave	Millimeter wave
MUSIC	Multiple signal classification
MSE	Mean squared error

MAE	Mean absolute error
PO	Physical optics
RAD	Range-azimuth-Doppler
RCS	Radar cross section
RGB	Red, green, blue
RMS	Root mean square
RTT	Round trip time
SAR	Synthetic aperture radar
SBR	Signal-based ray tracing
SNR	Signal-to-noise ratio
UR	Urban route
UTC	Coordinated universal time
UTD	Uniform theory of diffraction
UWB	Ultra wideband
V2I	Vehicle-to-infrastructure

List of Symbols

A	Amplitude of IF signal
α	Path loss intercept (AB model)
α_{PL}	One way free space loss f
b_{adc}	ADC resolution in bits
B	Bandwidth of chirp
β	is the path loss exponent‘
c	Speed of light in vacuum
γ	Coefficient representing frequency changes
d	Distance between radar and target
d_0	Reference distance
d_{max}	Maximum detectable range
Δd	Distance change
Δf	Frequency resolution or IF bandwidth
$\Delta\phi$	Phase difference
$\Delta\tau$	Time delay between Tx and Rx
f	Frequency
f_c	Carrier frequency
f_{IF}	Intermediate frequency (beat frequency)
F	Noise figure
F_r	Frame rate
F_s	Sampling frequency of ADC
G_f	Forward path gain factor
G_p	Target gain factor
G_t, G_r	Transmit and receive antenna gains
$h(f, d)$	Channel gain at frequency f and distance d
$h(t, \tau)$	Channel impulse response in time domain
$H(t, f)$	Channel frequency response
$\hat{P}_{\text{noise}}$	Estimated thermal noise power
K	Number of clutter clusters (in k-means clustering)

k_B	Boltzmann constant
λ	Wavelength of radar signal
N	Number of chirps per frame
N_{cell}	Number of CA-CFAR cells
N_f	Number of frames
N_s	Number of samples per chirp
P_r	Received power
P_t	Transmit power
P_{FA}	Probability of false alarm
P_{out}	Output power in dBFS or dBm
R	Estimated range
R^2	Coefficient of determination for path loss model fitting
S	Chirp slope
S_τ	Signal power from target on window (in clutter separation)
T	Antenna temperature or measurement duration
T_c	Chirp time
T_f	Total frame duration
T_{adc}	ADC start time
T_{idle}	Idle time
T_{meas}	Measurement interval
T_{ramp}	Ramp end time
τ	Round-trip time delay
ϕ_i	Initial phase of the i-th signal component
v	Velocity of the object
$\hat{v}$	Estimated velocity
v_{res}	Velocity resolution
w_i	Window coefficient for FFT
x_i	Value of the i-th reference cell in CA-CFAR window
$x_{\text{out}}(t)$	Mixer output signal as a function of time
X_{FI}, σ	Log-normal shadowing variable and standard deviation
$y(f, d)$	System gain in dB as a function of frequency and distance
Z	CFAR scaling factor

PL_{FI}	Floating Intercept (AB) path loss model value
$PL_{one-way}$	One-way (single-trip) path loss
$PL_{two-way}$	Two-way (round-trip) path loss
R_x	Receive antenna
T_x	Transmit antenna

1 Introduction

Radars are essential in various applications. That is the case of weather monitoring, where they help identify rainfall patterns and track storms and predict dangerous weather phenomena, thus improving safety conditions for the public (Holleman, Huuskonen, Kurri, & Beekhuis, 2010; Sokol et al., 2021). Also, the automotive sector relies on radars for crucial functions such as collision avoidance technology facilitating safer driving conditions (Aydogdu, Keskin, & Wymeersch, 2021; Rameez, Pettersson, & Dahl, 2022). Automotive radars (AR) are one of the important sensors of automotive technology. It helps the safety features such as adaptive cruise control (ACC), automatic emergency braking (AEB), and many more in both autonomous vehicles and traditional vehicles advanced driver assistance (ADAS) (Feng, 2025; Sharifisoraki, Amini, & Rajan, 2024).

A radar transmits electromagnetic waves and analyzes the corresponding echoes, those signal components are reflected by the objects in the environment. The echoed signals are processed to obtain information such as speed, distance, and direction of the objects in the environment (Prokopovich, Popov, Pajewski, & Marciniak, 2017).

There are multiple types of radar systems, differing in their functional methods and deployment fields. Pulsed radars transmit signals in discrete bursts, while continuous wave (CW) radars emit a continuous signal and detect changes in signal frequency for motion monitoring (Ahmed, Kallu, Ahmed, & Cho, 2021; Ha, Lee, Kim, & Baek, 2018). In addition, radars can also be characterized based on the spatial arrangement of the transmitter and receiver, such as monostatic, multistatic, and synthetic aperture radars (SAR). In monostatic radar systems, the transmitter and receiver are in the same position, whereas multistatic systems have separate transmitter and receiver stations, and have enhanced detection range due to its ability to view target from multiple geometric orientations (Boutkhil, Driouach, & Khamlichi, 2018; Inggs, Griffiths, Fioranelli, Ritchie, & Woodbridge, 2014; Lambot et al., 2004). Furthermore, high-resolution imaging is possible through SAR systems, due to signal processing enhancements that function regardless of weather

conditions (Soumya, Krishna Mohan, & Cenkeramaddi, 2023). In addition to structural classifications, radar systems can be distinguished by the principles of their operation, as well as certain advanced features. For example, medical applications use ultra wideband (UWB) radar that uses extremely short pulses in a wide spectrum to track vital signs and generate diagnostic-quality images, utilizing high-resolution scans. Furthermore, multiple input-multiple output (MIMO) radar technology has great potential through spatial diversity, which helps resolve radar system limitations such as multipath fading (Li, Wang, Yang, & Fu, 2021).

Understanding the environment can help to assess the impact of obstacles on signal behavior (Ji, Xue, Chen, & Wang, 2024). Moreover, the environment provides valuable information regarding signal propagation characteristics, such as multipath propagation (arrival of delayed, phase-shifted signals), Doppler effects (frequency shifts due to object motion), obstructions, and environmental noise that can affect received radar signals (Fens, Ruggiano, & Leus, 2008; Guo, Sun, Yang, & Fu, 2017; H.-N. Wang, Huang, & Chung, 2017).

This thesis focuses on AR applications that mostly depend on millimeter-wave (mmWave) radar technology. Such systems normally rely on the frequency-modulated continuous wave (FMCW) signals due to their high range resolution and tracking of moving targets in dynamic driving situations. FMCW radars have low power consumption, compact design, and high resolution (Gupta, Rai, Kumar, Yalavarthy, & Cenkeramaddi, 2021; Soumya et al., 2023). It works by continuously sending out frequency-modulated signals and analyzing the reflected echoes. It can measure range, velocity, angle of arrival (AOA) of the target in their detection range. The mmWave FMCW radar bandwidths is in several GHz and can detect objects from centimeters to several hundred meters. The radar data is mostly processed into 3D range-azimuth-Doppler (RAD) tensors, which contain information about object movement and distance. To extract the required information from the raw data, techniques such as fast fourier transform and multiple signal classification (MUSIC) are used (Sharifisoraki et al., 2024).

However, the overall performance of radar systems deteriorates because of different environmental and operational elements such as interference and clutter from unwanted echoes produced by land, sea disturbances, unwanted objects, atmospheric disturbances, and external electromagnetic interferences. The weather-related effects like rain attenuation and changing raindrop distribution patterns can further complicate radar operations (Li, He, Wang, Tang, & Hou, 2017). Other issues include receiver noise and external signal interference, both of which compromise the accuracy of the measured data (Pralon, Pompeo, & Fortes, 2015).

Note that the received radar signal captures the influence of the environment on signal transmission, and thus can be used to infer channel propagation characteristics. A channel model is a simplified mathematical representation of real-world communication channels, capturing signal characteristics such as path loss and time delay, which enable target position and movement assessment (Daniel & Popescu, 2012). Therefore, channel modeling requires evaluating the propagation environment to develop realistic signal representations that support both theoretical analysis and practical system deployment (Jiang, Mukherjee, Zhou, & Lloret, 2021).

Channel modeling can optimize communication processes by predicting channel behavior for specific terminals (X. Wang et al., 2024). While channel modeling is an established topic in radar and communication systems, most of the current techniques require detailed system-level or fixed deployment details. Limited research explores channel characteristics like the path loss, that can be estimated from radar data without full system knowledge. This reveals fundamental research gap, calling for simplified radar-based channel modeling approaches.

Furthermore, with a channel model in place, one can improve the radar's signal processing capabilities efficiently by filtering out noise sources, differentiating between closely spaced objects, and improving accuracy in identifying object properties (e.g., range, velocity, and angle). Apart from this, in autonomous systems such as vehicle-to-vehicle (V2V) communication, these models can help enhance navigation and obstacle avoid-

ance by providing real-time details of signal propagation influenced by the environment (Kumari, Choi, Gonzalez-Prelcic, & Jr, 2017). Moreover, Son, Sung, and Heo (2018) have explained the challenges of radar to radar interference in automotive systems and the need for better signal processing methods and channel modeling in real-world scenarios. In addition, the usage of FMCW radars for indoor operations such as unmanned aerial systems requires precise channel modeling techniques for navigation and obstacle detection, regardless of environmental conditions, according to (Scannapieco, Renga, & Moccia, 2015). Also for internet of things (IoT) smart cities (e.g., traffic management systems), channel models inferred from radar signals can help with better communication management, particularly in dynamic environments with varying obstacles or interference (Zhang, Li, & Wenger, 2020).

1.1 Research Objectives

The primary goal of the research is to propose a framework for channel modeling from radar signal data. Such a framework can help support various applications, such as optimizing communication processes, creating models or simulations that replicate how environmental elements affect radar signal characteristics, and improving the interpretation and processing of radar signals. The goals include:

- To gain a deeper understanding of the effects of environmental features (e.g., multipath propagation, Doppler effects, obstacles, etc.) on signal behavior, as observed through radar data.
- To derive a data-driven channel model using radar measurements using radar signal measurements, aiming for accurate representation of the physical environment.
- To validate the proposed statistical channel modeling through a proper characterization of the signal attenuation.

1.2 Thesis Outline

This thesis is organized as follows:

Chapter 1 provides the introduction and a contextual overview of the research area. It also presents the research objectives and motivation behind the study, also gives the outline of the thesis.

Chapter 2 gives the background of the FMCW radar and discusses the related work to the channel modeling. The basic concepts that are explored in Chapter 2 are the fundamentals of FMCW radar, cell averaging constant false alarm rate(CA-CFAR) detection, and channel modeling and measurement techniques for FMCW radar.

Chapter 3 explores the steps for estimation of the path loss from FMCW radar data. This includes feature extractions from radar data like range, velocity, and angle. It also explains the implementation of CA-CFAR detection for target and clutter identification and their separation. Afterward, it covers the path loss estimation from the radar data, including specific models for target and clutter.

Chapter 4 provides the results and analysis. It evaluates the path loss models performance. The chapter discusses the limitations of the current method and suggests improvements for future work.

Chapter 5 concludes the thesis with a summary of the key findings of the thesis.

2 Background

This chapter covers the basics of FMCW radar, including discussion on how signals are detected, and how the environment affects them. It also looks at different ways to model wireless channels.

2.1 FMCW Radar

An FMCW radar transmits a specific signal known as a chirp, which is a sinusoidal wave with a frequency that increases linearly over time. It is presented in an amplitude vs time plot in Figure 1a, where the signal changes in frequency while maintaining a consistent amplitude. From the frequency vs. time plot in Figure 1b, we can observe frequency shifts over time. Figure 1 also shows that linear frequency variation of the chirp signal results in sawtooth like frequency pattern.

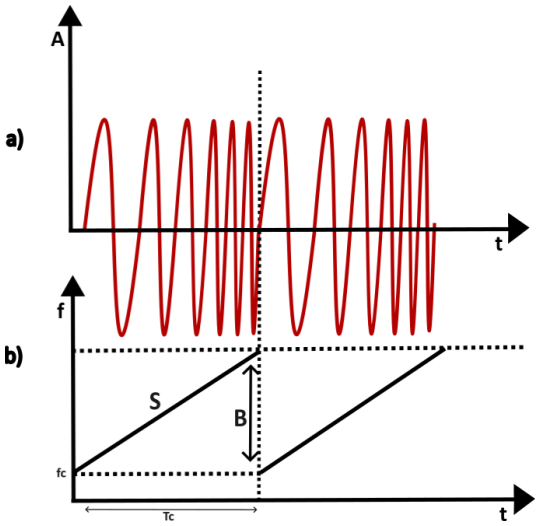

Figure 1. Chirp Signal. a) represents the amplitude-time domain, and b) represents the instantaneous frequency-time domain.

We can observe that a chirp can be described by four parameters: i) Firstly, start frequency (f_c) or ramp start, which is the initial frequency value; ii) next, the bandwidth (B),

which is the total frequency range during a chirp; iii) and chirp duration (T_c), which represents the chirp cycle time; iv) and slope (S) of the chirp defines the rate at which the chirp ramps up Bhutani et al. (2019), and is given by

$$S = \frac{B}{T_c}. \tag{1}$$

The operation of a simple 1- transmitter and 1-receiver ($1T_x$-$1R_x$) FMCW radar is illustrated in Figure 2. A synthesizer generates the chirp waveform, which is transmitted by means of a T_x antenna. The R_x antenna detects a time-delayed version of the transmitted chirp because the signal takes time to reflect off objects in the surroundings before it returns. The delay duration carries information about the actual distance from the radar to reflected objects. The received chirp after passing through the low-noise amplifier (LNA), is mixed with the transmitted chirp in the mixer. This step generates intermediate frequency (IF) signal. Finally, to remove the high-frequency components, the IF signal goes through low-pass filtering and is then digitized using an analog-to-digital converter (ADC). Then, digital signal processing (DSP) techniques extract object attributes such as range, angle, and velocity (Ramasubramanian, 2017; Rao, 2017). The upcoming sections will discuss this in detail.

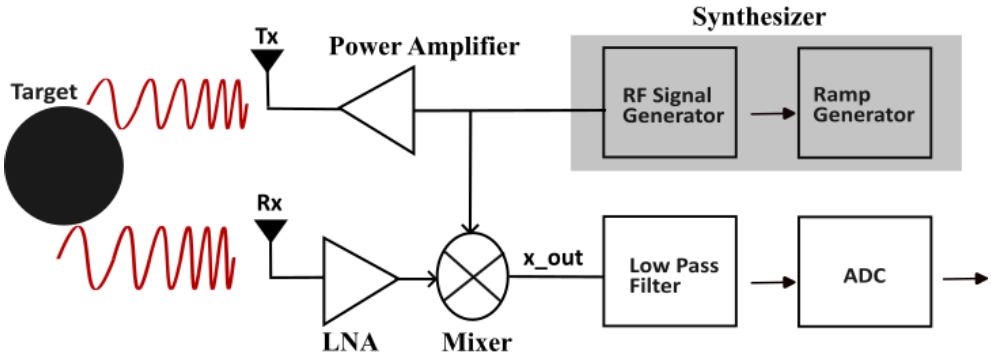

Figure 2. FMCW radar signal workflow.

2.1.1 Range Estimation

The IF signal contains information of the object's range, which is the distance between the radar module (containing transmitter and receiver antennas) and the measured object.

The output (x_{out}) from the mixer for two sinusoids can be modelled as

$$x_{\text{out}}(t) = \sin\left[2\pi(f_1 - f_2)t + (\theta_1 - \theta_2)\right], \tag{2}$$

where f_1 and θ_1 are the instantaneous frequency and phase of the transmitted signal, and f_2 and θ_2 are those of the received signal, respectively. From this, we can observe that the output sinusoid has an instantaneous frequency and phase equal to the difference of the frequencies and phases of the two input sinusoids, as presented in Figure 3. Here, a single object in front of the radar produces an IF signal with a constant frequency of $S\tau$, where τ denotes the round-trip time (RTT) between the radar and the object.

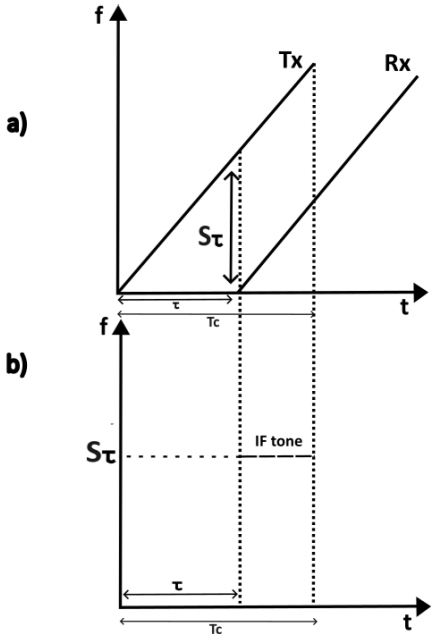

Figure 3. In a single-target measurement, (a) shows the frequency-time domain representation of both the transmitted and received signals, while (b) presents the frequency-time characteristics of the IF tone.

As mentioned in Scherr et al. (2017) we can write

$$\tau = \frac{2d}{c}, \tag{3}$$

where d is the range of the object and c is the speed of light. So, the IF tone can be expressed as

$$\mathsf{f}_{\mathsf{IF}} = S\tau = \frac{2Sd}{c}. \tag{4}$$

If there are multiple objects in front of the radar, then there will be multiple reflected chirps at the Rx antenna. A frequency spectrum of the IF signal will display multiple tones, each corresponding to the range of the object from the radar, as illustrated in Figure 4.

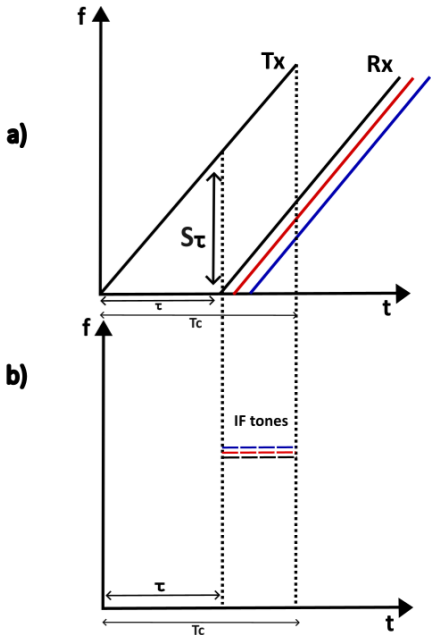

Figure 4. In a multi-target measurement, (a) shows the frequency-time domain representation of both the transmitted and received signals, while (b) presents the frequency-time characteristics of the IF tone.

For accurate range detection, two important parameters are considered: Range resolution and detection range.

Range resolution refers to the radar's ability to differentiate two closely spaced objects, and it depends upon B. A larger bandwidth B results in finer resolution (Park, Kim, Jung, & Lee, 2022). The frequency resolution of time-limited signals is given by $\frac{1}{T_c}$ according

to Fourier transform theory. Furthermore, the range of objects in the FMCW radar corresponds directly to the frequency of the IF signal according to the definition of the beat frequency. By using (3), the range resolution Δd can be expressed as (Nguyen, Nhat, & Huynh, 2014)

$$\Delta f > \frac{1}{T_c} \Rightarrow \frac{2S\Delta d}{c} > \frac{1}{T_c} \Rightarrow \Delta d > \frac{c}{2ST_c} \Rightarrow \frac{c}{2B}, \tag{5}$$

where $B = ST_c$.

Note that the maximum detection range depends on the highest IF. However, recall from the operation of FMCW radar in Figure 2, that the IF is digitized (LPF+ADC) for further processing on a DSP. So, the IF bandwidth is limited by the ADC sampling rate (F_s), and by using the beat frequency definition, the maximum range of the radar is given by

$$d_{\text{max}} = \frac{F_s c}{2S}. \tag{6}$$

2.1.2 Velocity Estimation

The FFT technique used for range estimation of multiple targets can experience limitations when two targets have identical distances and distinct velocity rates because the radar system cannot separate their signals. The frequency transform produces one peak in the IF signal while the two objects maintain the same range position. The range domain cannot separate the velocities of these objects by itself. Therefore, in such scenarios, the phase of the IF signal becomes essential for estimating the velocity of targets. Figure 5 illustrates for a single target scenario that the phase of the signal at the mixer output is the difference of initial phases of two inputs as expressed in (2).

The velocity estimation in FMCW radar depends on the analysis of phase changes be-

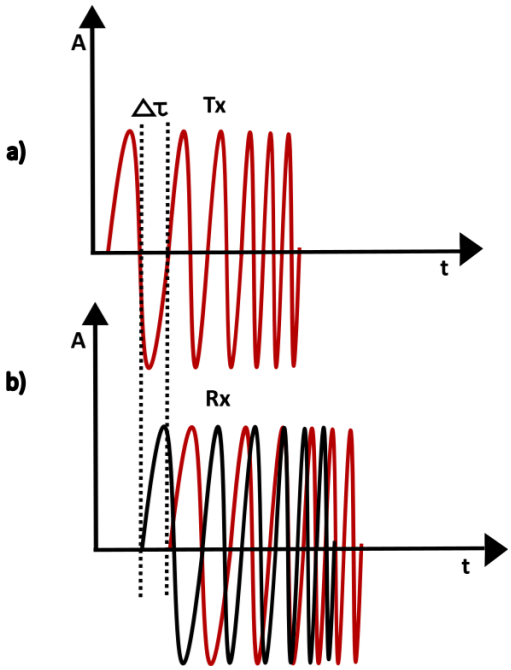

Figure 5. The representation of Tx and Rx signals following a time shift of $\Delta\tau$.

tween successive chirps of IF signal that result from Doppler effect. When the target is moving with a relative velocity with respect to the radar, the receiver will experience a time shift, $\Delta\tau$, while the transmitter will accumulate an additional phase shift of $2\pi f_c \Delta\tau$ (Rao, 2017). So, the sinusoidal IF signal will be $A\sin(2\pi f_{\text{IF}} t) + \phi_i$, where A is the amplitude, f_{IF} can be defined using (4), and ϕ_i is the initial phase. Using $c = f_c\lambda$, where λ represents the radar's wavelength, the phase difference can be expressed as

$$\Delta\phi = 2\pi f_c \Delta\tau = \frac{4\pi\Delta d}{\lambda}. \tag{7}$$

Considering that multiple chirp signals are separated by T_c, the phase difference measured across two consecutive chirps can help find the velocity of the target (v). The travel distance can be represented as $\Delta d = vT_c$. Thus (7) transforms into

$$v = \frac{\lambda\Delta\phi}{4\pi T_c}. \tag{8}$$

Now, let us consider the case of a multiple-object scenario, in which there are two (or more) objects that have the same distance from the radar but have different relative velocities. Similar to a single object, they will have one IF tone. However, this tone contains distinctive phase information for each object. So, to separate the targets, a Doppler FFT is applied to the series of the range FFT peaks, which correspond to N transmitted chirps. This is illustrated in Figure 6, wherein we can see that each peak in the Doppler FFT represents the phase difference from the distinct object.

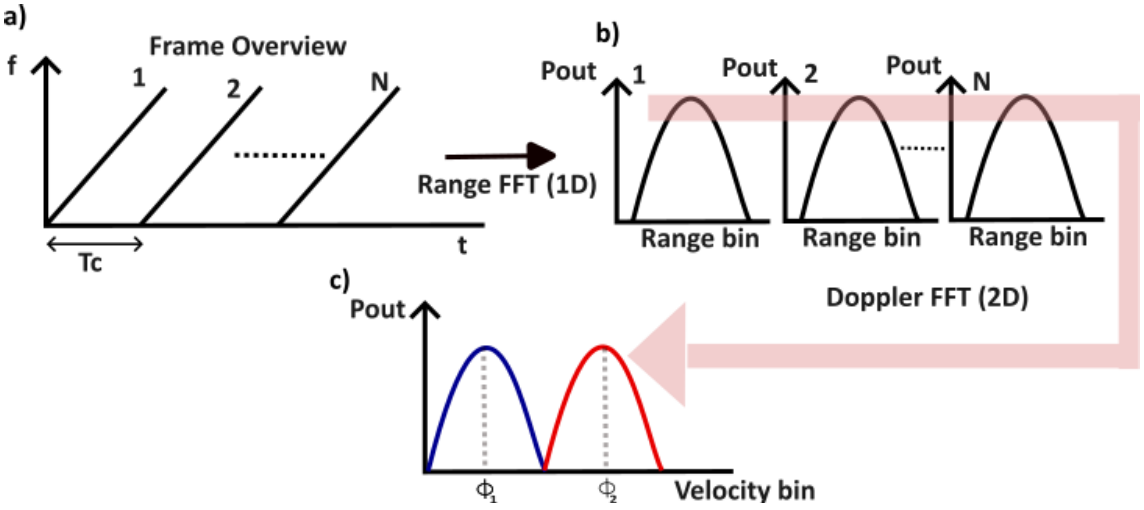

Figure 6. Velocity estimation of multiple targets using 2D FFT in an FMCW radar system. (a) The frame overview shows a sequence of N transmitted chirps separated by the period T_c. (b) A 1D FFT is applied across each chirp to obtain range profiles, resulting in distinct range bins. (c) A 2D Doppler FFT is then performed across multiple chirps within each range bin to resolve velocity information, allowing the separation of targets located at the same distance but with different relative velocities..

Using (8), the relative velocities of two targets can be expressed as

$$v_1 = \frac{\lambda \Delta \phi_1}{4\pi T_c}, \quad v_2 = \frac{\lambda \Delta \phi_2}{4\pi T_c}, \tag{9}$$

assuming that both objects are moving toward the radar.

The two main concepts related to velocity estimation feasibility are velocity resolution

and maximum velocity. Velocity resolution defines the smallest velocity difference between objects that can be detected. The calculation of velocity resolution depends on the phase difference between successive chirps. From (7) combined with the discrete nature of the signal, demonstrates that the two frequency components can be resolved if their phase difference satisfies

$$\Delta\phi > \frac{2\pi}{N}, \tag{10}$$

using this together with phase-velocity relationship, we obtain

$$v > \frac{\lambda}{2NT_c}. \tag{11}$$

Finally, by expressing the total frame duration as $T_f = NT_c$, the velocity resolution can be calculated as

$$v_{\text{res}} = \frac{\lambda}{2T_f}. \tag{12}$$

On the other side, maximum unambiguous velocity denotes the highest detectable relative velocity which avoids phase ambiguity between consecutive chirps. According to (Wan, Song, Mu, & Wang, 2019), the phase difference must remain below π radians ($\Delta\phi < \pi$) for unambiguous velocity estimation. Relating phase difference to velocity, we get

$$v < \frac{\lambda}{4T_c}. \tag{13}$$

Thus, the maximum unambiguous velocity is expressed as

$$v_{\text{max}} = \frac{\lambda}{4T_c}. \tag{14}$$

Finally, angle estimation is required specially when multiple objects share the same range and velocity. For this, one can use antenna spacing to obtain angular separation through signal phase comparison. This signal direction estimation technique known as AoA operates with minimum two receiver antennas and employs Fourier-based methods to determine incoming signal directions (Li et al., 2021). Although AoA helps resolve spatial ambiguity, it was not implemented in this thesis.

2.1.3 Signal-to-Noise Ratio

The signal-to-noise ratio (SNR) is defined as the ratio between the power of the received signal and the background noise (Rao, 2017). It is defined as:

$$SNR = \frac{P_{\text{r}}}{P_{\text{noise}}}, \tag{15}$$

where P_{r} is the power received from the target at R_x antenna, and P_{noise} is the power of unwanted background noise. To analyze SNR in radar applications, the received power can be derived using the two-way radar equation (Rao, 2017). The two-way radar equation (also called the radar range equation) expresses the power received by a radar system after a signal is transmitted, reflects off a target, and returns to the radar. It's called "two-way" because the signal travels to the target and back, so the distance attenuation happens twice. It can be expressed as

$$P_r = \frac{\sigma_{\text{RCS}} P_t G_t G_r \lambda^2}{(4\pi)^3 d^4}, \tag{16}$$

where σ_{RCS} is the radar cross-section (RCS) of the target, P_t is the transmitted power, G_t is the transmitter antenna gain, and G_r is the receiver antenna gain. Figure 7 illustrates the components and physical interpretation of the two-way radar equation for better

understanding.

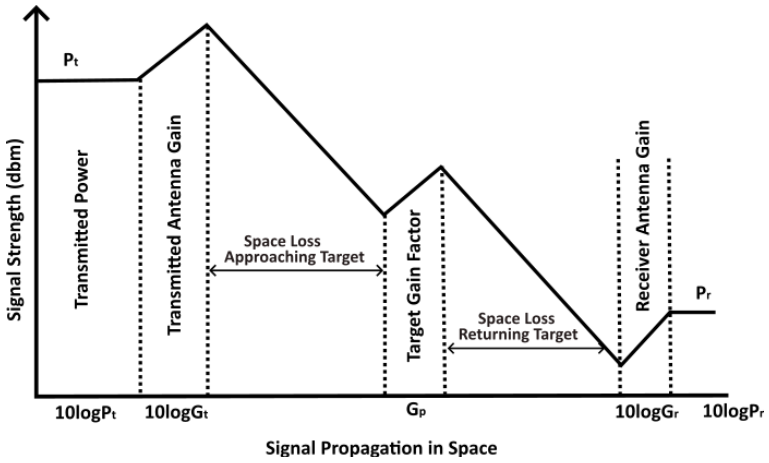

Figure 7. Radar signal strength variation from transmission to reception, highlighting transmitter power, antenna gains, space losses, and target reflection.

The two-way radar equation can be rewritten in logarithmic form as

$$10 \log P_r = 10 \log P_t + 10 \log G_t + 10 \log G_r + G_p - 2\alpha_{PL}, \tag{17}$$

where G_p is the target gain factor that shows how much radar signal is reflected back from a target, based on its σ_{RCS}, and α_{PL} represents the one-way free space loss. The two main sources of noise in radar systems are thermal noise and radar clutter. Thermal noise is uniformly distributed across the frequency spectrum. Radar clutter, on the other hand, is divided into mainlobe and sidelobe clutter. Mainlobe clutter arises from unwanted ground reflections within the radar beamwidth, while sidelobe clutter results from returns outside the main beam, often dominated by ground reflections or side objects other than the target at short ranges. The background noise power is modeled as Nyquist thermal noise, which is given by

$$P_{\text{noise}} = k_B T \Delta f, \tag{18}$$

where k_B is the Boltzmann constant, T is the antenna temperature, and Δf is the bandwidth. Note that this expression accounts only for thermal noise and does not include clutter power, which may also contribute significantly to the overall noise in practical

radar systems. For a more accurate SNR estimation, system losses must be considered. Substituting (16) and (18) into (15), the SNR can be rewritten as:

$$SNR = \frac{\sigma_{\text{RCS}} P_t G^2 \lambda^2 T_{\text{meas}}}{(4\pi)^3 d^4 k_B T F}, \tag{19}$$

where G represents the antenna gain, $T_{\text{meas}} = \frac{1}{\Delta f}$ represents the measurement period, and F represents the system's noise figure that accounts for losses in antenna networks and associated components.

2.2 CA-CFAR Detection

In radar systems, a detection decision needs to be made before extracting useful information. This process is complicated by the presence of interfering signals. CFAR analyzes the received signal, which includes target reflections and interference, and compares its amplitude with a predefined threshold. If the signal exceeds this threshold, a detection is recorded, but it may not necessarily be from the target. False alarm occurs when the background noise or interference exceeds the set threshold, leading to incorrect detections. A CFAR detector calculates the mean power of noise and interference and adjusts the threshold accordingly. Each cell under test (CUT) receives a threshold value from surrounding cells, which represents specific resolution areas in range, Doppler, or angle parts of radar data (Richards, Scheer, & Holm, 2010).In radar signal processing, a cell refers to a discrete resolution bin in range, Doppler, or angle, each containing a signal amplitude or power value. These cells form the basic units over which detection decisions are made.

Various CFAR methods exist, each having different processing capabilities, and are mentioned by Richards et al. (2010). One of these, introduced by Finn and Johnson, is the CA-CFAR technique, which is widely used for radar signal detection. In this method, using the reference window, the noise level estimate $\hat{P}_{\text{noise}}$ is derived. It consists of N_{cell} surrounding cells denoted as $\{x_i\}_{N_{\text{cell}}}$, where N_{cell} represents the total number of reference cells, and x_i are the values of individual cells within the window, which represents

the signal power levels from surrounding reference cells used to estimate the noise level and set a detection threshold for the CUT.

So, the detection threshold T is defined by multiplying the noise estimate $\hat{P}_{\text{noise}}$ and the predefined scaling factor Z, expressed as:

$$T = \hat{P}_{\text{noise}}\, Z \tag{20}$$

A target is detected if the signal level in the test cell exceeds T. The noise level $\hat{P}_{\text{noise}}$ is estimated as the sample means of the reference cells around the test cell:

$$\hat{P}_{\text{noise}} = \frac{1}{N_{\text{cell}}} \sum_{i=1}^{N_{\text{cell}}} x_i \tag{21}$$

The scaling factor Z can be calculated as

$$Z = N_{cell} \left(P_{FA}^{\frac{1}{N_{cell}}} - 1 \right), \tag{22}$$

where P_{FA} is the desired probability of false alarms. The CA-CFAR cell division is shown in Figure 8.

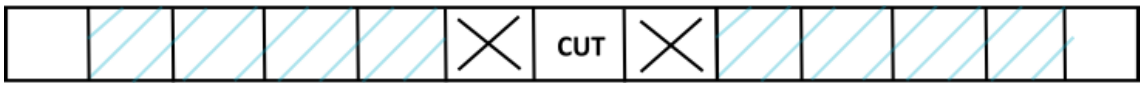

Figure 8. CA-CFAR cell division. The shaded cells represent reference cells for noise estimation, the ”X” cells are guard cells, and the central CUT (cell under test) is evaluated for target presence..

Guard cells are the immediate neighboring cells around the CUT. They are not included in averaging because the target reflections are spread over many samples, so including these samples in the average will increase the threshold and potentially reduce detection sensitivity.

2.3 Propagation and Channel Models

Electromagnetic wave propagation depends upon the transmission medium through which they travel, and that medium between the transmitter and the receiver is called the communication channel. In radar systems, this channel includes the path to the target and back, making the understanding of two-way propagation effects essential. The strength and the quality of the received signal directly depend upon the characteristics of the propagation mechanism. The received signal at the receiver may consist of multiple components that travel different paths with varying time delays because of effects like reflection, diffraction, and refraction. Understanding the propagation mechanism is necessary for designing and optimizing radar systems (Samad, Choi, Kim, & Choi, 2023).

In an ideal free-space scenario, an electromagnetic wave will travel in a straight line without obstruction, experiencing distance-dependent attenuation due to the spreading of energy over distance. This behavior is captured by Friis transmission equation, which models free space path loss (FSPL) as

$$\mathrm{PL}_{\mathrm{FSPL}} = \left(\frac{4\pi d}{\lambda}\right)^2 . \tag{23}$$

However, when the signal travels through a real-world wireless channel, it experiences various environmental obstacles such as buildings, trees, and people. In radar applications, these also include targets like vehicles, aircraft, or ships. Reflection occurs when the radar signal encounters a smooth surface that is larger than its wavelength. Main sources of reflection include the ground, buildings, and indoor structures like walls, floors, and ceilings. Diffraction in radar occurs when radar waves bend around obstacles such as mountains, buildings, or ships. Scattering occurs when the radar wave interacts with objects that are smaller than its wavelength, such as dust particles, rain droplets, or rough surfaces (Fuschini et al., 2008). Multipath propagation refers to scenarios where the transmitted signal reaches the receiver through multiple routes due to reflection, diffrac-

tion, and scattering (Xiongwen Zhao & Vainikainen, 2001). The various versions of the same signal arrive with different delays, amplitudes, and phase shifts. They may either strengthen the received signal or weaken it, leading to multipath fading. In radar, this can lead to fluctuations in target detection accuracy or even false alarms due to constructive and destructive interference.

2.3.1 Two-way Radar Channel

The radar channel is inherently bidirectional and involves signal propagation from the radar to the target and back. Figure 9 illustrates this two-way path loss model for a radar system (Gil, Lee, & Cho, 2021).

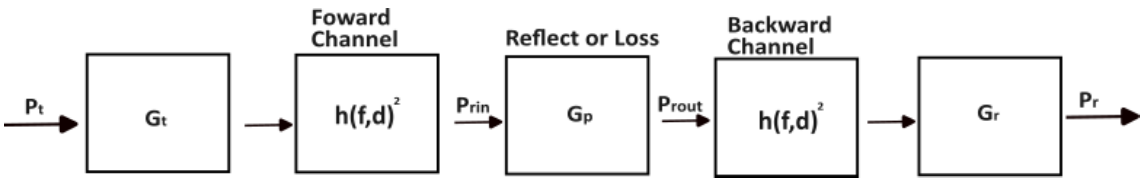

Figure 9. Two-way path loss model for a radar system.

In this model, the signal undergoes attenuation in both the forward path (radar to target) and the backward path (target to radar). The signal power at various stages can be characterized as follows

The power of the signal reaching the target via the forward path is

$$P_{r,in} = P_t G_t |h(f,d)|^2, \tag{24}$$

where $|h(f,d)|^2$ is the channel gain for a specific frequency f and distance d. The target reflects or re-radiates this incoming power with a gain factor G_p, which gives us

$$P_{r,out} = P_{r,in} G_p = P_t G_t G_p |h(f,d)|^2. \tag{25}$$

Finally, the power received by the radar receiver through the backward propagation path

becomes

$$P_r = P_{r,out} G_r |h(f,d)|^2 = P_t G_t G_p G_r |h(f,d)|^4. \tag{26}$$

The total radar system gain, defined as the ratio of received power to transmitted power, can be expressed in logarithmic form as

$$y(f,d) = 10 \log_{10} \left(\frac{P_r}{P_t} \right). \tag{27}$$

Substituting (26) into (27) and simplifying:

$$y(f,d) = 10 \log_{10}(G_t G_p G_r) + 10 \log_{10} |h(f,d)|^4. \tag{28}$$

The one-way path loss is:

$$PL_{one-way}(f,d) = -10 \log_{10} |h(f,d)|^2, \tag{29}$$

substituting (29) into (28) and rearranging, we obtain:

$$PL_{one-way}(f,d) = \frac{10 \log_{10} \left(\frac{G_t G_p G_r P_t}{P_r} \right)}{2}. \tag{30}$$

For signal propagation prediction, several path loss models are being used widely according to the environment and the frequency ranges. These models help in evaluating how signal power degrades over distance, especially in complex environments where clutter and obstructions are present. The floating intercept (FI) model also known as alpha-beta (AB) model, is flexible in fitting measurement data with adjustable slopes and intercepts (Gil et al., 2021). It is also used in this thesis. This model, as defined in the standards of the

WINNER II and 3rd generation partnership project (3GPP), is mathematically expressed as (Z. Wang, Li, Liu, & Wang, 2024)

$$\mathrm{PL}_{\mathrm{FI}}(d) = \alpha + 10\beta \log_{10}\left(\frac{d}{d_0}\right) + X_{\sigma}^{\mathrm{FI}}, \quad d \geq d_0. \tag{31}$$

Here, d_0 is the reference distance, which is taken as 1 m normally. The term α is the floating intercept in dB, and β is the path loss exponent that characterizes the rate at which path loss increases with distance. The random variable X_{σ}^{FI} is for large-scale fading and follows a log-normal distribution with zero mean and a standard deviation of σ (in dB). In this thesis, we assume that α aggregates wideband effects, even though it may vary across frequency ranges, while β remains constant within the modeled band. For radar systems, although the FI model does not directly incorporate radar-specific parameters, it is still useful for empirical modeling of propagation loss in cluttered or indoor radar environments.

An extension to the FI model is the alpha-beta-gamma (ABG) Model, which incorporates the frequency dependence as well (Sun et al., 2016). An extension of the AB model is the ABG model, which incorporates both distance and frequency dependence. It is useful for modeling large propagation across several frequencies and environments. The ABG model is defined as (Erunkulu, Zungeru, Thula, Lebekwe, & Mosalaosi, 2024):

$$PL_{\mathsf{ABG}}(f, d) = 10\alpha \log_{10}\left(\frac{d}{d_0}\right) + \beta + 10\gamma \log_{10}\left(\frac{f_c}{1\,\mathsf{GHz}}\right) + X_{\mathsf{ABG}}^{\sigma}, \quad d \geq d_0. \tag{32}$$

Here, γ coefficient represents changes according to frequency and $X_{\mathsf{ABG}}^{\sigma}$ represents large-scale fading in the ABG model that has a zero mean depending on the σ. The importance of this model is maximized in scenarios where signal performance has distinctly variable

behaviors across different frequency bands. In the case of the ABG model, the frequency effect is explicitly captured by γ and f_c, but similar to the previous model, challenges remain when dealing with wideband systems. Selecting the right model depends on factors like environment (urban, rural, indoor), frequency band, and desired accuracy.

2.3.2 Modeling Techniques for Radar Propagation Channels

Channel modeling in the real world facilitates theoretical analysis, performance evaluation, and deployment of wireless communication systems by providing an accurate representation of wireless propagation (Jiang et al., 2021). Different channel modeling methods exist that group into deterministic models and statistical models. Depending on radar sensing requirements, these modeling approaches provide distinct characteristics which make them appropriate for various applications.

Physical-deterministic modeling uses the laws of physics, especially how electromagnetic waves behave, to predict how signals travel in a specific, known environment. This is called a site-specific approach because it relies on detailed information about the place where the signal is being sent. If we know everything about the surroundings, we can use this information to accurately simulate or predict how the signal will move and behave. The deterministic modeling is classified within these methods, known as geometric methods and numerical methods. Geometric methods, including geometric optics (GO), physical optics (PO), uniform theory of diffraction (UTD), and signal-based ray tracing (SBR) operate efficiently when the target dimensions surpass radar wavelength thresholds (Wei et al., 2024). The precise calculations of complex target shapes through numerical methods like the method of moments (MoM) and fast multipole method (FMM), together with finite-difference time-domain (FDTD) require high computational costs (Wei et al., 2024). The accuracy level of deterministic models produces exact signal estimates suitable for scenarios that need precise channel descriptions. Their advanced computational needs make it difficult to use them in real-time to monitor dynamic physical environments. However, precise detailed data is required when working with deterministic modeling tech-

niques.

Statistical modeling is used when there is limited knowledge about the propagation environment or the physical processes occurring within it. This situation arises either when detailed information about the environment is unavailable or when the goal is to describe general propagation behavior across a category of environments rather than a specific one. Empirical statistical models rely on measurements of the overall outcomes of the propagation process, without focusing on the underlying physical details. These models can describe the statistical distribution of parameters like path loss for a given type of environment. As a result, it's essential to classify the environment before conducting empirical observations and developing the model. One advantage of statistical modeling is that it can work with the least information, however, it requires a large amount of data to model the statistical characteristics of propagation parameters (path loss and fading and delay spread) within a given environment category. Radars detecting multiple independent scatterers as targets, can provide a statistical representation of the target distribution. Statistical models adapt well to different conditions, although they need significant datasets to represent data accurately.

Recently, a hybrid modeling approach has received attention for radar channel modeling. This approach uses both deterministic and statistical methods to model clutter and the target σ_{RCS}. For example, X. Wang et al. (2024) have used a hybrid channel modeling, using deterministic modeling for σ_{RCS} modeling and statistical modeling for the side clutter. Apart from this, Liu et al. (2024) have also introduced a hybrid modeling approach in which target and clutter data are separated. Liu et al. (2024) have then modeled the σ_{RCS} of the target by using RT, and on the other hand, it has modeled the path loss from the clutter signal through a statistical method. This methodology increases radar simulation precision by providing high-resolution deterministic techniques that are applied for detailed modeling of significant components of the target. On the other hand, simplistic statistical models are applied for clutter, which still offers a high simulation fidelity by reducing overall computational requirements. So, hybrid methodologies have been proven effective for precise and efficient V2X channel modeling according to X. Wang et

al. (2024) and Liu et al. (2024).

2.4 Channel Impulse Response

The channel impulse response (CIR) characterizes how an impulse signal propagates through an environment by capturing time delays, amplitudes, and phases of multipath components (X. Wang et al., 2024). CIR analysis provides essential quantitative details about multipath propagation behavior and thus enables both precise simulation models and system optimization in changing environments (Liu et al., 2024). Information in the CIR allows mmWave radar devices to identify different objects using echoes returned from objects (Liu et al., 2024). The CIR in V2X communication allows for observing signal-object interactions and detecting targets more precisely and pinpointing their exact locations (X. Wang et al., 2024). Signal quality is determined by the strength and delay of multipath components thus, precise CIR modeling is crucial for reliable sensing and communication systems (Liu et al., 2024). The channel impulse response can be derived from the channel's frequency response through the implementation of the inverse fast fourier transform (IFFT). This relationship is expressed as

$$h(t,\tau) = \mathsf{IFFT}\{H(t,f)\}. \tag{33}$$

CIR appears in the time-delay domain as $h(t,\tau)$, while $H(t,f)$ represents the channel frequency response. The time-domain characteristics of CIR are influenced by path loss and Doppler shift effects, which become important in mmWave channels due to their significant signal attenuation (Liu et al., 2024). To model CIR, both path loss and path gain play an important role. Path gain is the inverse of the path loss (in linear scale), which indicates how much of the transmitted signal power is retained at the receiver.

3 Path Loss Estimation from FMCW radar data

This chapter focuses on estimating path loss using FMCW radar data in a V2I communication setup. It presents a detailed testbed overview, signal pre-processing, and methods for identifying, separating, and modeling radar reflections from targets and clutter to estimate the signal attenuation.

3.1 V2I Radar Testbed and Data Collection Setup

The scenario and dataset based on vehicle-to-infrastructure (V2I) communication are selected from (Alkhateeb et al., 2023). The testbed is illustrated in Figure 10 and includes a stationary base station, which is referred to as unit 1, and a mobile unit, referred to as unit 2. The former includes a red, green, blue (RGB) camera (StereoLabs ZED 2), light detection and ranging 2D (LiDAR) (SLAMTEC RPLiDAR), FMCW radar (TI AWR2243BOOST), 60 GHz mmWave phased array receiver (Sivers EVK06002), and global positioning system (GPS) receiver (SparkFun RTK2). Meanwhile, the latter utilizes an omnidirectional 60 GHz mmWave transmitter together with a GPS receiver.

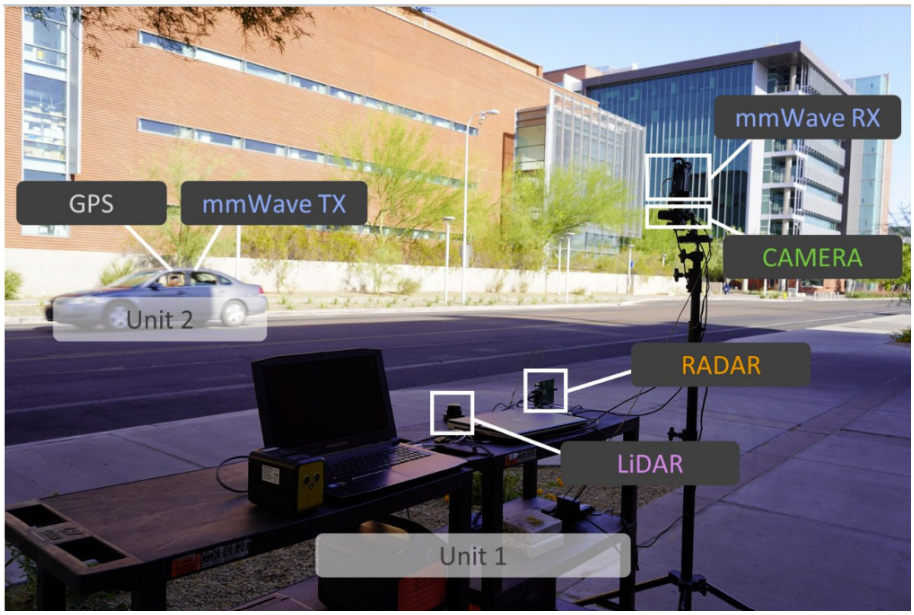

Figure 10. Testbed for recording radar data, taken from (Alkhateeb et al., 2023).

This data was collected during the day on McAllister Avenue, a two-way street with two lanes, 10.6 meters wide, and a speed limit of 25 mph (40.6 km/h). The testbed was set up near the entrance of a parking lot. This area includes cars, pedestrians, and cyclists, making it a good example of real-world conditions. All sensors are synced using timestamps at about 10 times per second to keep the data consistent. The FMCW radar can detect objects up to 100 meters away. Figure 11 from the dataset helps to visualize the environment in which the data is collected.

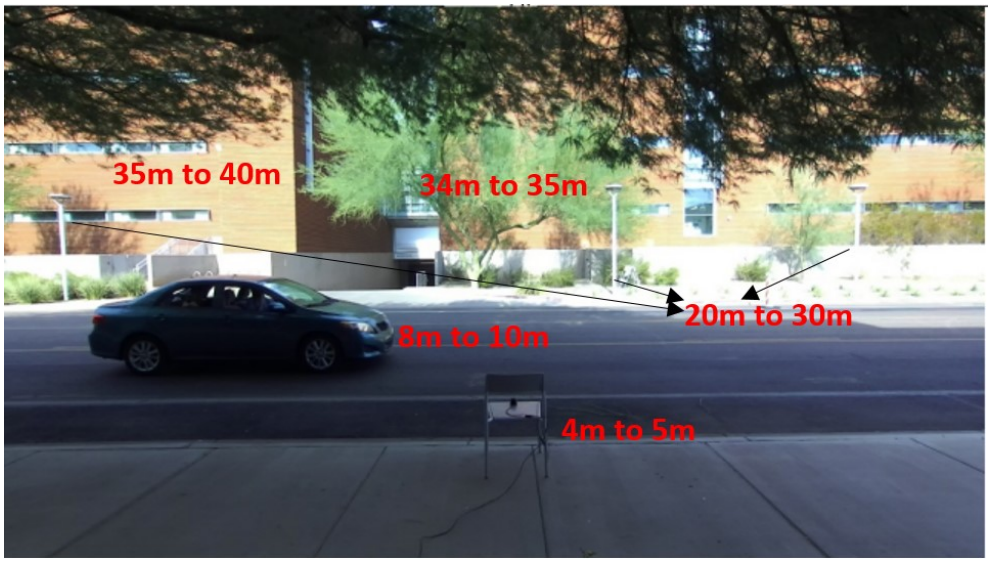

Figure 11. Measurement environment on McAllister Avenue (Alkhateeb et al., 2023). It shows the urban setting where the data was collected, featuring both static objects and the target along with approximate distances.

The environment includes both static objects, which contribute to clutter in the measurements, and the moving vehicle on the road, which serves as the target in our data. The sources of clutter include the chair, trees overhead, poles across the road, trees near the building, and the building itself. The mix of moving vehicles and static objects in this urban setting creates a variety of reflections and signal blockages. However, the minimal moving clutter apart from the main vehicle can help to model path loss accurately in this scenario.

The datasets provided by Alkhateeb et al. (2023) for different scenarios have already been used in applications such as radar-aided beam prediction, user identification and

positioning, and blockage detection (Alkhateeb et al., 2023; Charan, Alrabeiah, Osman, & Alkhateeb, 2023; Morais, Behboodi, Pezeshki, & Alkhateeb, 2022). These data sets enable real-world research by integrating multimodal sensing techniques with wireless communication, offering realistic, synchronized, large-scale measurements.

The used radar is AWR2243BOOST, and its specifications are mentioned in (Texas Instruments, 2024). Here, it is worth noting that the datasheet specifies 3 T_x antennas; however, the (Alkhateeb et al., 2023) data set uses only one of those T_x antennas for measurements. The frame structure is shown in Figure 12. Parameters used from the datasheet are provided in Table 1.

Table 1. Radar Parameters.

Parameter (Symbol)	**Value**
Number of transmit antennas (N_{TX})	1
Number of receive antennas (N_{RX})	4
Transmit and receive antenna gains ($G_\mathrm{t}, G_\mathrm{r}$)	10.85 dBi
Transmit power (P_t)	13 dBm
Samples per chirp (N_s)	256
Chirps per frame (N)	128
Sampling frequency (F_s)	5000 Ksps
Carrier frequency (f_c)	77 GHz
Chirp slope (S)	15.015 MHz/μs
Frame structure	$4 \times 256 \times 128$
Total number of frames (N_f)	5,964
Ramp end time (T_ramp)	60 μs
ADC start time (T_adc)	6 μs
Idle time (T_idle)	5 μs
Frame rate (F_r)	10 frames per second

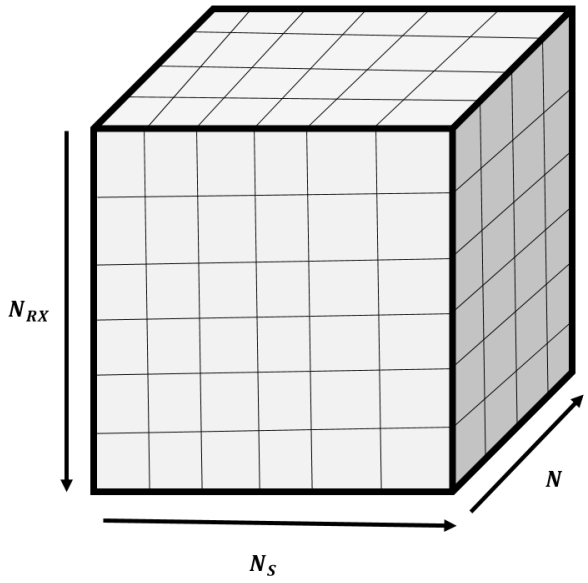

Figure 12. Radar data cube structure representing the three-dimensional organization of received radar signals. The axes correspond to the number of receiving antennas (N_{RX}), the number of chirps or slow-time pulses (N_S), and the number of fast-time samples per chirp (N).

3.2 Pre-processing for Feature Extraction

In this section, the data sources and pre-processing steps applied to radar data before path loss estimation are discussed.

3.2.1 Range Estimation

The range is calculated by applying a 1D FFT to the received radar signal, which is initially in the time domain. The range FFT is applied on a per-chirp basis using the ADC samples collected during each chirp. A Hamming window is applied to the ADC data before the FFT to reduce spectral leakage. Each discrete frequency element in the FFT spectrum represents a particular beat frequency associated with its index k. This beat frequency corresponds to a specific distance, as each point in the frequency spectrum maps to a distinct range from the radar. The estimated range corresponding to the index k, denoted

as R_k , can be calculated using (5). The heat map for range estimation for one sample is shown in 13. The range FFT shows reflections at different distances, yet not every peak indicates a valid target. Next, the system applies a CA-CFAR algorithm to eliminate noise while better identifying meaningful reflection.

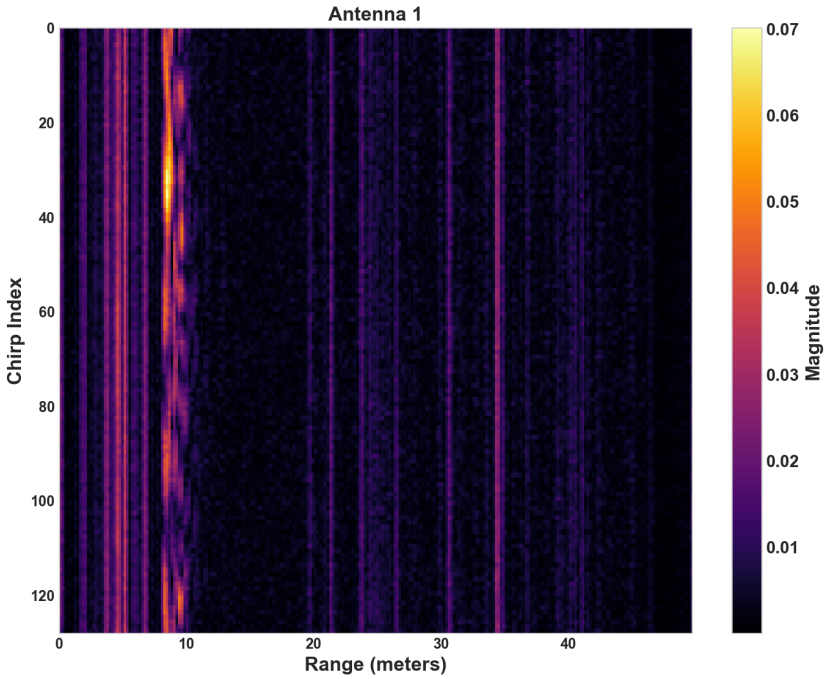

Figure 13. Range heatmap for one sample.

3.2.2 CFAR Implementation

For CA-CFAR, the 1D FFT matrix is taken as the input. The size of the CA-CFAR window is user-configurable according to need. For our scenario, 3 guard cells and 12 training cells are selected for the sliding window. The P_{FA} is set to be 0.09, and the scaling factor is calculated from (22). The CA-CFAR window is applied to the 1D FFT matrix row-wise. The resultant matrix with the average energy of every cell of the 1D FFT matrix is then multiplied with a scaling factor to compute the threshold matrix, which defines the detection threshold for each cell. This threshold matrix is then compared against the original 1D FFT matrix, and any cell with a value exceeding the threshold is identified as a potential target. CA-CFAR is applied separately to each of the four antennas for each frame. The results for one sample for one antenna after the CA-CFAR detections is shown in Figure

14.

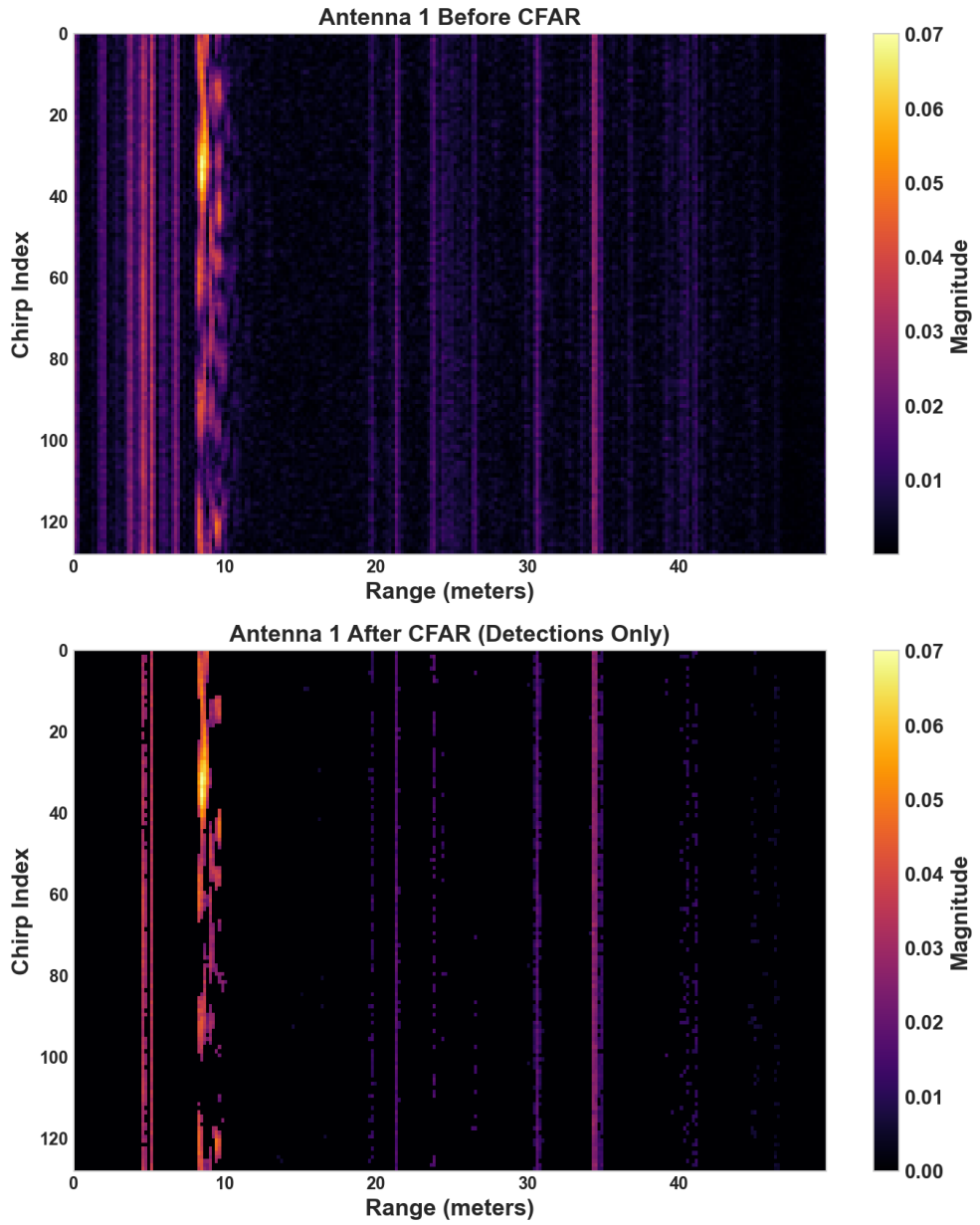

Figure 14. Before and after CFAR results on range FFT for one sample.

3.3 Target and Clutter Identification

After the implementation of CA-CFAR, the range-time plot is generated from the radar data. Comparing the Figure 11 with the Figure 15, we can relate the peaks with the target and clutter. Note that the peak that is being observed at the distance of 4–5 m is due to

the chair as it is constant across all chirps when the data is observed for 5s in Figure 15. Similarly, the peaks after 20 m are consistent, which contain peaks due to poles, trees, and the building. The target is located at a range between 8 m and 10 m. Its movement can be observed in Figure 15, where it appears between 8 m and 10 m over the 5-second data interval. The results were confirmed with a comparison across all four antennas.

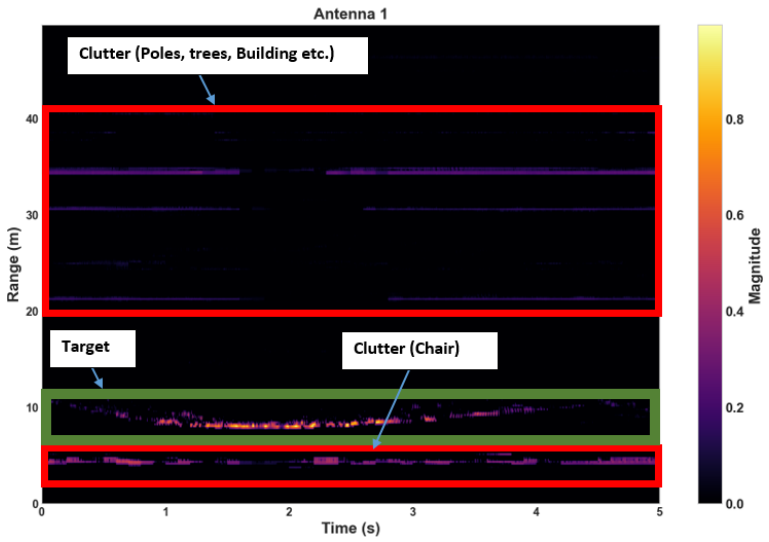

Figure 15. Range-time Heatmap from Antenna 1 showing stationary environmental clutter (upper and lower red box), a moving target at (green box).

3.4 Target and Clutter Separation

To separate the clutter and the target after identification, the Doppler information from the range-Doppler data has been used. As we know, in our scenario, clutter is referred to as stationary objects in the environment, so their reflection will exhibit nearly zero Doppler shift. However, the moving object, such as the target in our scenario, has a non-zero Doppler shift due to its motion relative to the radar. So, the separation step involves analyzing the velocity axis of the range-Doppler matrix. By detecting velocity changes within the Doppler bins, the object's motion was observed in a specific range region. This allowed the object's range to be estimated based on its velocity, distinguishing it from surrounding clutter.

3.4.1 Velocity Estimation

For velocity estimation, a second FFT is applied across the slow-time axis (pulse dimension), similar to how the first FFT is applied across fast-time samples for range estimation. This step, often referred to as Doppler-FFT, involves applying a 2D FFT to the 1D FFT range estimation results by performing a Doppler FFT across the chirps in the frame for each receiver. It is then shifted to center the zero Doppler frequency, to ensure that zero frequency (no velocity) is in the center, with negative and positive velocities evenly distributed around it. By doing this, we can capture the phase differences between chirps, which helps in velocity estimation. The rows of the resultant Doppler FFT matrix represent the range bins, and the columns represent the velocity bins. The Range-Doppler matrix provides a 2D representation of detected targets, which maps their respective distances and velocities. The velocity resolution, which determines the spacing between each velocity bin in the output, is calculated using (12) and the full velocity range spans from $-v_{\text{res}}\frac{N}{2}$ to $+v_{\text{res}}\frac{N}{2}$. The range-Doppler heatmap for the first 50 frames, corresponding to a 5-second range-time profile, is shown in Figure 16. For each frame, the chirps in all four antennas are averaged to obtain a single representative point. These points are plotted on the right side within the estimated range region highlighted on the left side of Figure 16. The rest of the range data is considered static clutter with zero velocity.

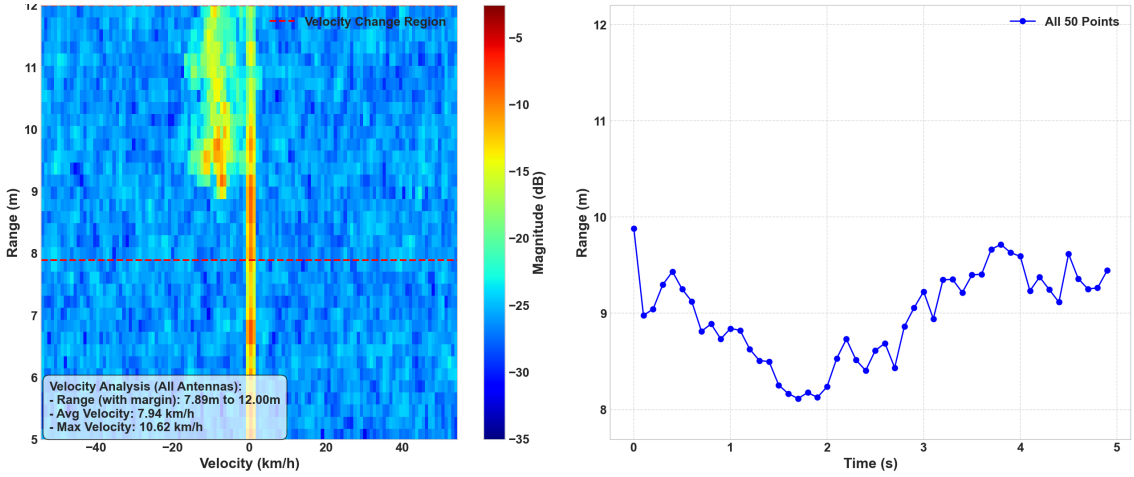

Figure 16. The left plot shows the Range-Doppler map obtained using a 2D FFT across fast-time and slow-time, where the highlighted region indicates target motion with a velocity change between 7.89 m and 12 m. The right plot displays the tracked range points over a 5-second interval for all four antennas.

3.5 Clustering for Clutter

From Section 3.3, we can identify the possible object, but we need a better classification method to analyze the environment. For clutter, equal distribution K-Means has been proposed for this thesis to evaluate the spatial patterns of clutter. This method is based on the K-means algorithm, in which the data is partitioned into groups. This is done by minimizing the distances between points and their assigned centroids that represent each cluster center. In K-means approach, the centroids are initialized randomly, which can generate unbalanced and biased cluster sizes, particularly when working with 1D data, such as in our case, the range values. However, in equal distribution K-Mean centroids are initialized using predetermined distances across the range of data to achieve balanced cluster distribution. The points for the target object within predefined minimum and maximum exclusion thresholds are omitted during the initialization process. Then, points are distributed to the nearest centroids based on range distance, and centroids are updated as the means of their assigned points. This clustering algorithm implements weighting using magnitude values that allow stronger signal reflections to influence the clustering more significantly. After clustering, the cluster labels, centroid positions, and average magnitudes of all points within the cluster are computed, which results in an organized grouping of clutter. Then different K values were implemented to achieve the best possible result.

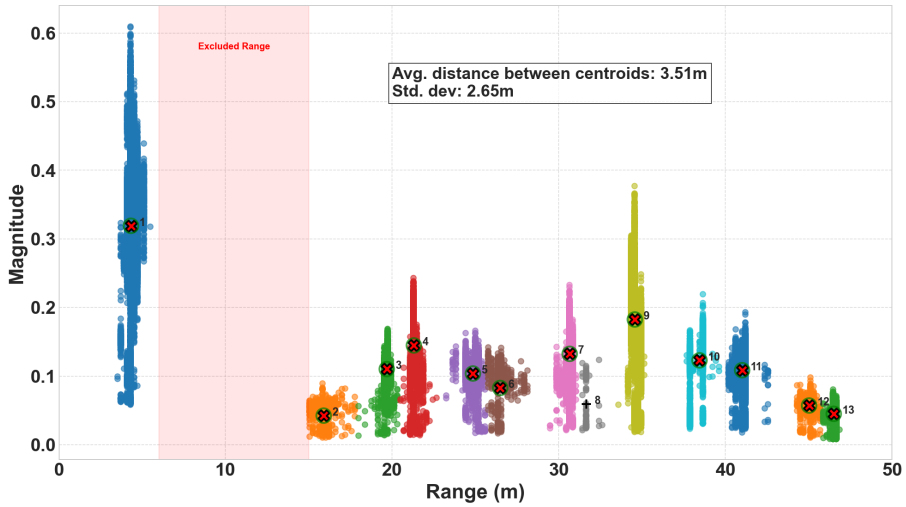

Figure 17. Clustering result when K=13, for first 50 frames for Antenna 1.

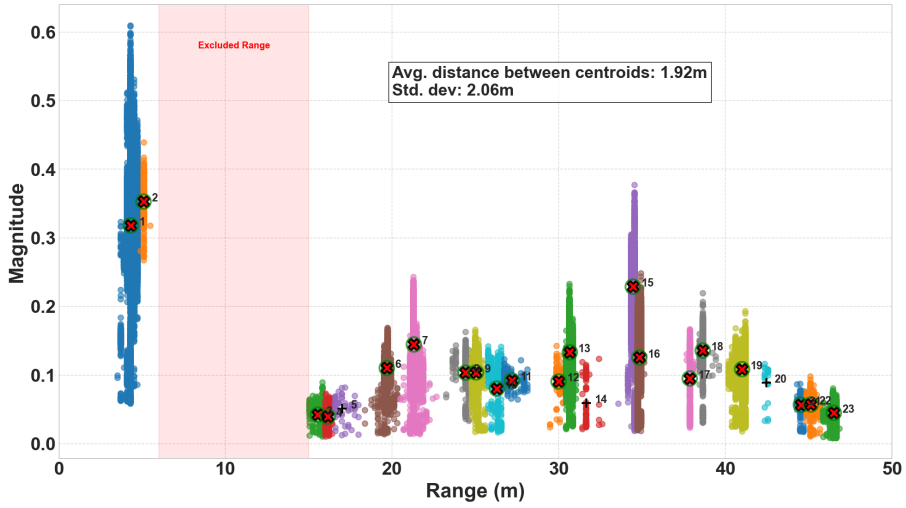

Figure 18. Clustering result when K=23, for first 50 frames for Antenna 1.

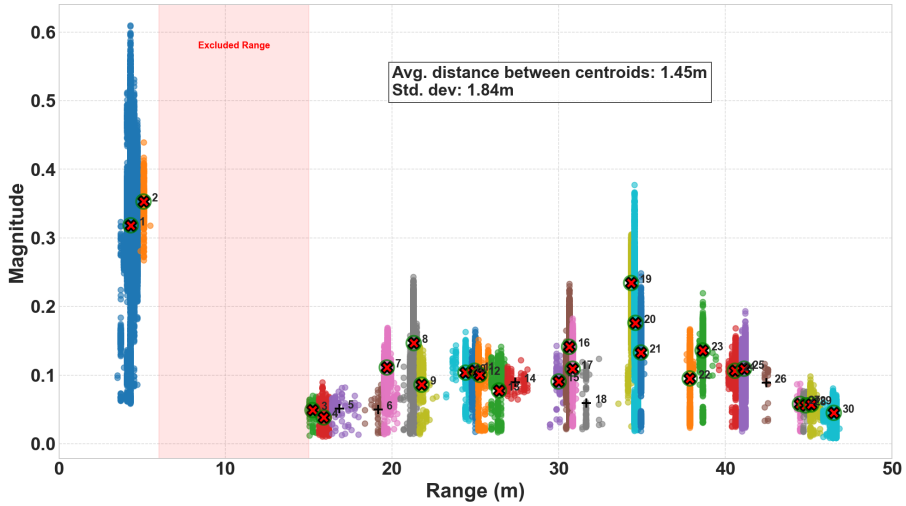

Figure 19. Clustering result when K=30, for first 50 frames for Antenna 1.

The Figures 17, 18, and 19 represent the clusters that are generated for the first 50 frames from the dataset for Antenna 1. Increasing the number of clusters from K=13 to K=30 results in more detailed and fine-grained grouping of the radar data. With K=30, the clusters are tighter and more localized, as shown by the reduced average distance between centroids (1.45m vs. 3.51m) and lower standard deviation (1.84m vs. 2.65m). This leads to better separation of closely spaced data points, making the clustering more precise. The higher K offers improved resolution. The summary of observations with different values of K is given in Table 2.

Table 2. Comparison of clustering results for different values of K.

Metric	**K = 13**	**K = 23**	**K = 30**
Avg. Distance Between Centroids	**3.51 m**	**1.92 m**	**1.45 m**
Standard Deviation of Distances	2.65 m	2.06 m	1.84 m
Cluster Spread (Beyond 15m)	Widely spaced	Moderately spaced	Closely spaced
Interpretation	Broad grouping, less resolution	Balanced detail	Fine-grained, more precise
Clarity in Static Clutter	Low	Medium	High
Best for General View	✓		
Best for Balanced Analysis		✓	
Best for Detailed Clutter Study			✓

After calculating the range and average magnitude values for each cluster per antenna, the final values for clutter were obtained by averaging these quantities across all four antennas over the entire dataset.

3.6 Target Trajectory Mapping Using Average Velocity Segmentation

To analyze the motion of a moving object after separation from clutter, velocity is estimated using Doppler-FFT. A single average velocity value has been estimated for the dataset and is used to determine the time required for a fixed distance calculation. The estimated velocity for the overall data is estimated as $\hat{v} = 3.05$ m/s. The estimated velocity for the first 50 frames is shown in Figure 20. The distance is kept constant at $d = 0.5$ m. The calculated time is 0.164 s. This time is then used to define data segments representing the object's travel range. From each segment, one average point is selected to represent the position of the object. This process was repeated across the dataset to map object movement. Figure 21 represents the averaged points after the first time-based segmentation for the first 50 frames from the dataset. Once all data points are computed for the complete dataset, they are grouped into range-based interval sets. The overall calculated range is segmented into intervals using a threshold of 0.3 meters. Within each interval, data points falling within the corresponding range boundaries are grouped together. The average range and magnitude are then recomputed for each interval. This will give 5 to 10 points representing the different ranges of the object with respect to the radar for complete data. Minimizing the number of data points reduces noise and redundancy, making the data cleaner and easier to interpret. It highlights key positional changes of the object

while maintaining the overall trend.

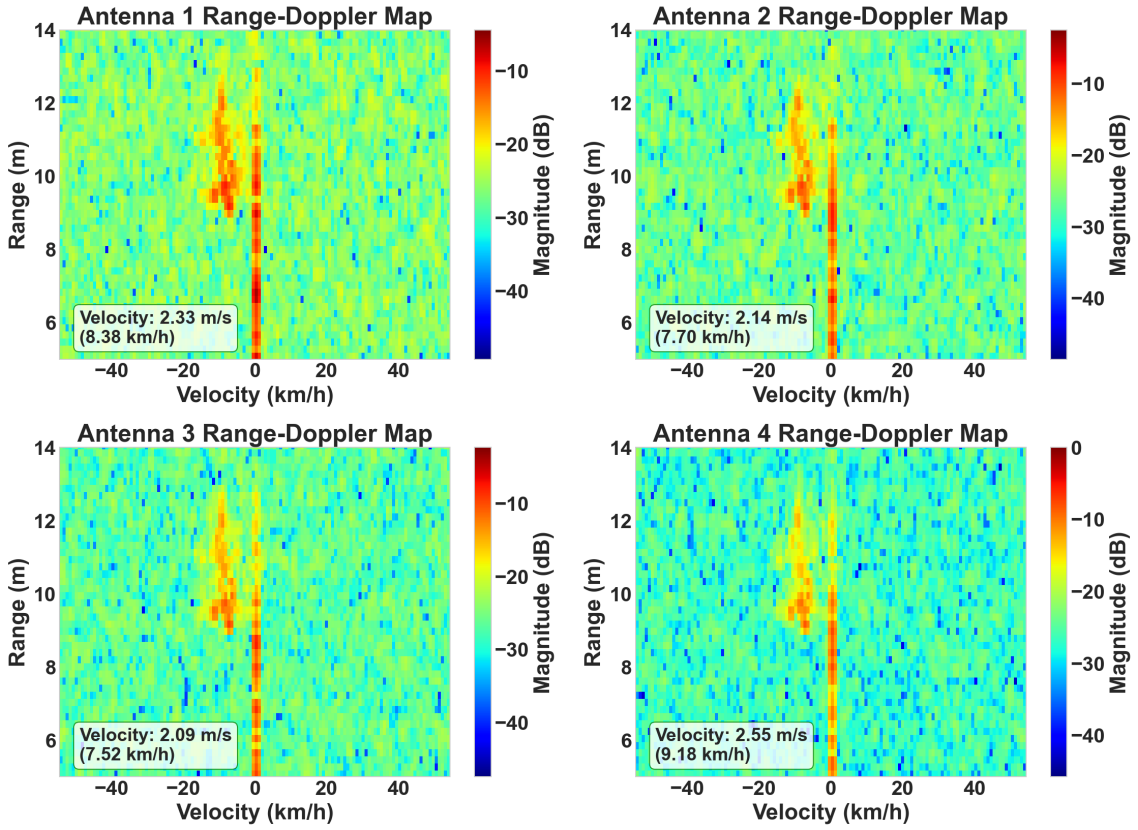

Figure 20. Estimated Average Velocity for 50 frames for all antennas, where combined $\hat{v} = 2.28\,\text{m/s}$.

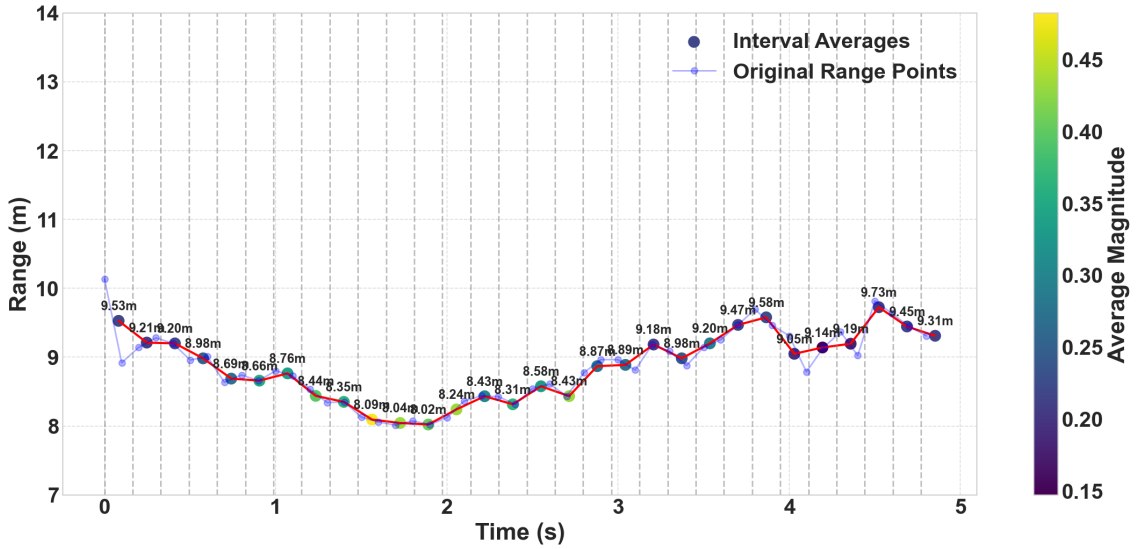

Figure 21. Range vs. time plot for first 50 frames showing time-based interval averages of range and average magnitude. Blue dots represent original range data points, red lines indicate interval averages, and the color gradient denotes average magnitude.

3.7 Path Loss Estimation

Path loss has been estimated from the extracted range FFT results. A correction factor is applied to raw ADC data before converting it to dBFs (decibels relative to full scale) because the raw FFT output doesn't directly represent power in a standardized dB scale (Texas Instruments, 2018). The correction factor consists of three components aiming to i) adjusts the raw digital output of the ADC to match the real-world signal range by scaling the values between ±1; ii) compensates for any attenuation caused by applying a window function; and iii) adjusts the FFT output to reflect the true power of a full-scale sine wave, which is measured using its RMS value.

$$P_{\text{r}}(\text{dBFS}) = P_{\text{r}}(\text{FFT}) - \left[20\log_{10}\left(2^{\text{bits}-1}\right) + 20\log_{10}\left(\sum_{i=0}^{N-1} w_i\right) - 20\log_{10}(\sqrt{2})\right], \quad (34)$$

$$P_{\text{r}}(\text{dBFS}) = P_{\text{r}}(\text{FFT}) - \text{Correction Factor}.$$

If no windowing is used, it means each window coefficient w_i is equal to 1. In that case, the sum of all window coefficients is simply N_s. For the studied dataset, where the ADC resolution is 12 bits (i.e., b_{adc}), the Hanning window over 256 N_s has a sum of approximately 128, thus, (34) is reduced to

$$\begin{aligned}\text{Correction Factor (dB)} &= 20\log_{10}(2048) + 20\log_{10}(128) - 3.01,\\ &= 105.35\,\text{dB}.\end{aligned}$$

As P_t is given in dBm, we have to convert P_r to dBm as well using (35). The constant value of 13 is added when converting from dBFs to dBm for a full-scale complex sinusoid because a complex signal has twice the power of a real signal due to having both In-phase (I) and Quadrature (Q) components. A real full-scale sinusoid of ± 1 V has an RMS (Root Mean Square) value of $1/\sqrt{2}$, which corresponds to 0 dBFs and is equivalent to 10 dBm. In contrast, a complex sinusoid with both I and Q at ± 1 V results in an RMS value of 1 V, which is 3dB in power. Therefore, a full-scale complex sinusoid corresponds to 0 dBFS =

13 (Texas Instruments, 2018).

$$P_{\mathrm{r}(dBm)} = P_{\mathrm{r}(dBFS)} + 13 \tag{35}$$

After we get the power in the dBm scale, we can use (17) to calculate the path loss. The rearranged formula for the path loss is given as follows:

$$\alpha_{PL} = \frac{1}{2}\left(10\log P_t + 10\log G_t + 10\log G_r + G_p - 10\log P_r\right). \tag{36}$$

The calculation assumes G_{P} to be zero because these values are not available. Determining the exact or precisely estimated values of these parameters is difficult and changes with the hardware and environmental conditions. This assumption introduces uncertainty but can be treated as random or uncontrollable factors. However, this assumption doesn't affect much the analysis of target and clutter path loss.

3.8 Path Loss Modeling for Target and Clutters

Once the path loss is calculated for clutter and target, a joined model is applied by plotting the path loss against distance. The AB and ABG path loss models are used to fit the measured path loss. To evaluate the accuracy of the path loss models, the following metrics are used: mean squared error (MSE), mean absolute error (MAE), maximum error (Max Error), and R-squared (R^2-Score).

The MSE quantifies the average of the squared differences between the actual and predicted path loss values, where n represents the total number of final calculated data points and is given by

$$MSE = \frac{1}{n}\sum_{i=1}^{n}(PL_i - \widehat{PL}_i)^2. \tag{37}$$

MAE represents the average of the absolute differences between the actual and predicted path loss value and is given by

$$MAE = \frac{1}{n}\sum_{i=1}^{n}|PL_i - \widehat{PL}_i|. \tag{38}$$

Max error gives the highest absolute deviation between the actual and predicted path loss values and can be calculated as

$$MaxError = \max(|PL_i - \widehat{PL}_i|) \tag{39}$$

The R^2 Score shows how well the predicted values account for the variance in the actual path loss data, given by

$$R^2 = 1 - \frac{\sum_{i=1}^{n}(PL_i - \widehat{PL}_i)^2}{\sum_{i=1}^{n}(PL_i - \bar{PL})^2}. \tag{40}$$

4 Discussion

This chapter presents a comparative evaluation of AB and ABG path loss models using radar data across varying clutter conditions. It also discusses the limitations of the current framework and outlines future directions for enhanced modeling in dynamic and multi-target environments.

4.1 Result Analysis

The fitted path loss curves along with corresponding confidence intervals and evaluation metrics (MSE, MAE, Max Error, σ, and R^2) for various scenarios, are illustrated in the subsequent figures. The AB and ABG model fittings for $K = 13$, $K = 23$, and $K = 30$ are shown in Figures 22, 23, and 24 .

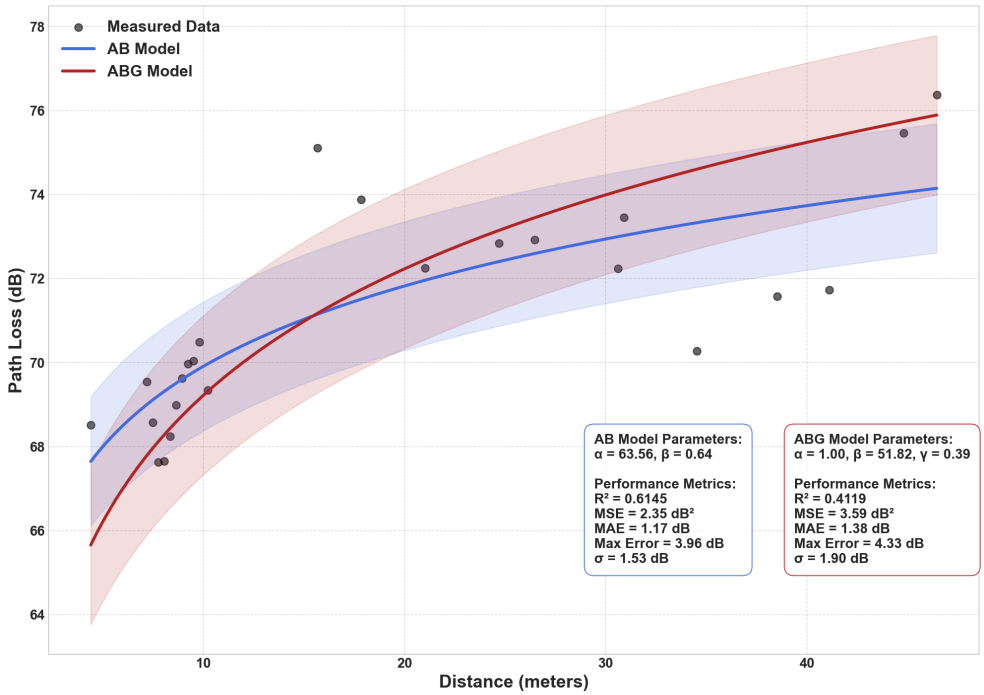

Figure 22. Comparative curve fitting of AB and ABG path loss models for K=13. The blue and red curves correspond to the AB and ABG models, respectively, with shaded regions indicating confidence intervals.

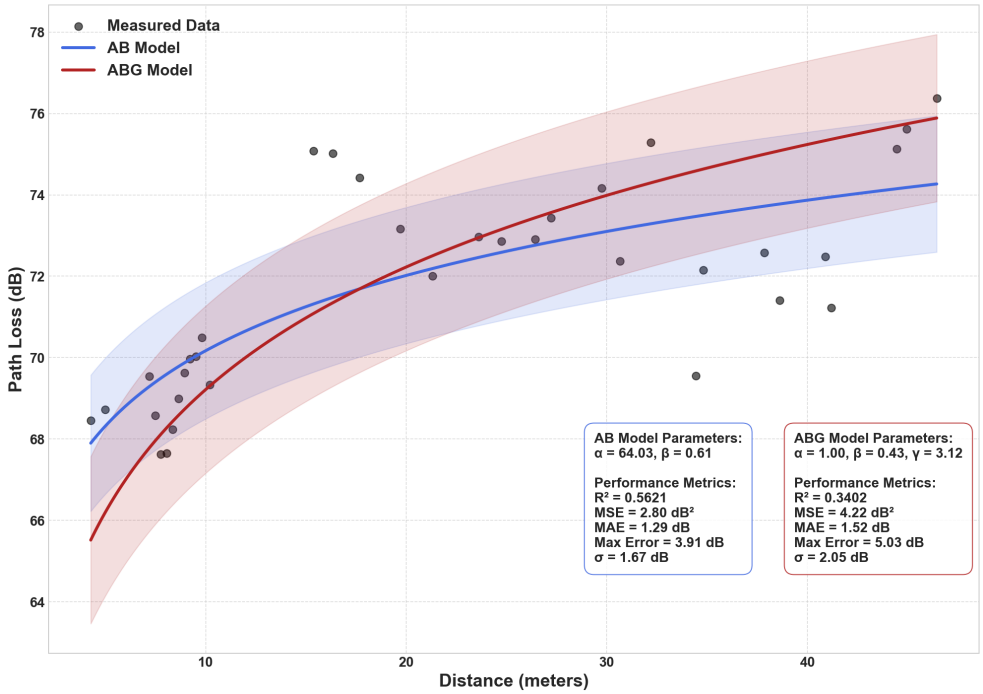

Figure 23. Comparative curve fitting of AB and ABG path loss models for K=23. The blue and red curves correspond to the AB and ABG models, respectively, with shaded regions indicating confidence intervals.

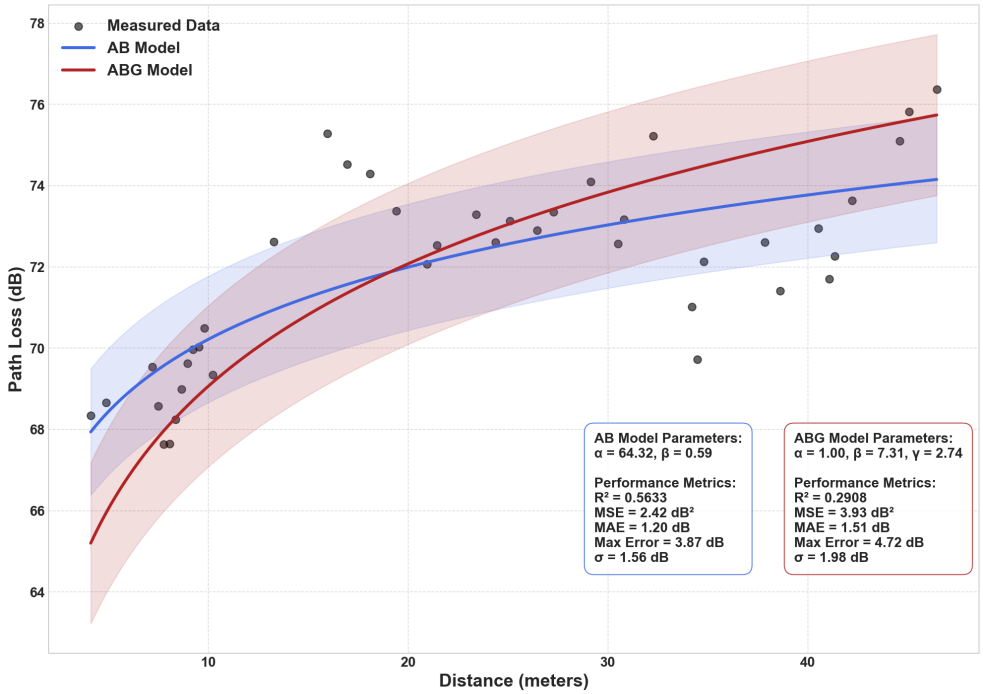

Figure 24. Comparative curve fitting of AB and ABG path loss models for K=30. The blue and red curves correspond to the AB and ABG models, respectively, with shaded regions indicating confidence intervals.

The comparative analysis between the AB and ABG path loss models in different clutter scenarios represented by varying K values shows a significant difference in model performance as presented in Table 3.

Table 3. Performance comparison of AB and ABG path loss models for different clutter clustering (K = 13, 23, 30).

Metric	**AB Model**			**ABG Model**		
	K = 13	K = 23	K = 30	K = 13	K = 23	K = 30
MSE	2.25	2.80	2.42	3.59	4.22	3.93
MAE	1.17	1.29	1.20	1.38	1.52	1.51
Max Error	3.96	3.91	3.87	4.33	5.03	4.72
σ	1.53	1.67	1.56	1.90	2.05	1.98
R^2	0.6145	0.5621	0.5633	0.4119	0.3402	0.2908

With an increase in K, the AB model shows superior generalization, which can be seen by a lower MAE and MSE across all scenarios compared to the ABG model. This shows that the AB model effectively captures the dominant distance-based propagation trend. Its reduced complexity helps maintain a smooth estimation curve.

In terms of residuals, σ of the AB model is consistently lower than that of the ABG model. This reflects the more stable and reliable error distribution of the AB model, with fewer extreme residuals. The maximum error for the AB model is also smaller, indicating that it experiences fewer large deviations from the actual path loss measurements. In contrast, the ABG model, which also includes frequency dependence, tends to show greater variability and higher errors in cluttered environments. Furthermore, R^2 is consistently higher for the AB model. The higher R^2 value indicates that the AB model explains a greater proportion of the observed path loss data, which makes it a better fit for the propagation trend. In comparison, the ABG model is not able to explain the variance as effectively, with lower R^2 values. This suggests that its predictions are more scattered and less consistent with the measured data.

The differences between the two models are also evident visually from Figure 22, 23, and 24. With narrower confidence intervals, the AB model displays smoother, more consis-

tent curves, indicating greater predictability. The ABG model, on the other hand, exhibits more pronounced fluctuations and a wider uncertainty band, indicating high sensitivity to clutter and overfitting. The wider confidence intervals suggest that the ABG model is less predictable and more prone to large errors due to clutter around the target region. In conclusion, we can say that the AB model outperforms the ABG model in all key performance metrics as K increases.

4.2 Limitations and Future Work

The developed model focuses on a scenario of a single moving target among stationary clutter, using a radar system consisting of 1 transmit and 4 receive antennas. This setup is according to the structure of the dataset and facilitates efficient single-target detection. However, the implementation of the model in situations with different targets (especially those with similar velocities), additional processing methods are needed to obtain adequate target separation capabilities and channel analysis. Furthermore, this model does an effective path loss estimation using radar data, but for detailed and precise analysis, σ_{RCS} is required. With σ_{RCS} information, we can model propagation conditions more precisely. Another limitation of this work is the averaging of received power over the entire wideband spectrum, which neglects frequency-dependent variations and may affect the accuracy of power-based analysis.

Even though the presented research concentrated on one target and stationary clutter, it provides a foundation for future multi-target scenarios through the use of enhanced signal processing techniques and angle-based separation. MIMO antenna configurations serve in this situation to extract spatial information, which enhances both angular resolution and more efficient separation between adjacent objects. Furthermore, situations can be considered where the radar system is moving. In such a scenario, the target and clutter become dynamic, requiring time-varying channel models. Furthermore, the application of machine learning and deep learning-based models presents opportunities to expand modeling capabilities for complex scenarios, which results in improved sep-

aration, tracking, and parameter estimation accuracy across different propagation conditions. These expanded models can facilitate useful practical applications within autonomous systems, together with smart cities, because they can improve the prediction of real-time propagation behavior, which is needed for reliable communication. In addition, to address the limitation of wideband power averaging, future work could involve dividing the spectrum into narrowband segments and estimating power separately for each, enabling frequency-selective analysis and more accurate propagation modeling.

5 Conclusion

A framework was developed to exploit FMCW radar to model signal propagation channels in actual outdoor environments. The study used radar-derived range and velocity, as well as signal strength data, to achieve accurate path loss estimation in V2I conditions for both targets and clutter. The research methodology includes with preprocessing to extract features, followed by CA-CFAR implementation for target and clutter detection, and application of path loss modeling for mobile and stationary objects.

Two path loss models, AB and ABG, were applied to fit the measured data. The analysis revealed that the AB model consistently outperformed the ABG model across all key performance metrics, including MSE, MAE, maximum error, standard deviation (σ), and R^2 score. The AB model demonstrated better generalization capability, smoother fitting curves, and narrower confidence intervals, indicating greater robustness and stability in varying clutter conditions. These results confirm the AB model as a more reliable choice for path loss estimation in the given radar-based scenario. The result demonstrated that FMCW radar measurements can effectively track signal attenuation effects from environmental factors. Thus, highlighting the feasibility of future radar-based channel models for communication systems.

Bibliography

Ahmed, S., Kallu, K. D., Ahmed, S., & Cho, S. H. (2021, February). Hand Gestures Recognition Using Radar Sensors for Human-Computer-Interaction: A Review. *Remote Sensing*, *13*(3), 527. https://doi.org/10.3390/rs13030527

Alkhateeb, A., Charan, G., Osman, T., Hredzak, A., Morais, J., Demirhan, U., & Srinivas, N. (2023, September). DeepSense 6G: A Large-Scale Real-World Multi-Modal Sensing and Communication Dataset. *IEEE Communications Magazine*, *61*(9), 122–128. (Conference Name: IEEE Communications Magazine) https://doi.org/10.1109/MCOM.006.2200730

Aydogdu, C., Keskin, M. F., & Wymeersch, H. (2021, January). Automotive Radar Interference Mitigation via Multi - Hop Cooperative Radar Communications. In *2020 17th European Radar Conference (EuRAD)*. Utrecht, Netherlands: IEEE. https://doi.org/10.1109/eurad48048.2021.00076

Bhutani, A., Marahrens, S., Gehringer, M., Göttel, B., Pauli, M., & Zwick, T. (2019, September). The Role of Millimeter-Waves in the Distance Measurement Accuracy of an FMCW Radar Sensor. *Sensors*, *19*(18), 3938. https://doi.org/10.3390/s19183938

Boutkhil, M., Driouach, A., & Khamlichi, A. (2018). Detecting and localizing moving targets using multistatic radar system. *Procedia Manufacturing*, *22*, 455–462. https://doi.org/10.1016/j.promfg.2018.03.070

Charan, G., Alrabeiah, M., Osman, T., & Alkhateeb, A. (2023, August). *Camera Based mmWave Beam Prediction: Towards Multi-Candidate Real-World Scenarios*. arXiv. (arXiv:2308.06868 [cs]) https://doi.org/10.48550/arXiv.2308.06868

Daniel, A., & Popescu, D. C. (2012, March). A vector channel approach to waveform design for radar systems. In *2012 46th Annual Conference on Information Sciences and Systems (CISS)* (pp. 1–5). Princeton, NJ, USA: IEEE. https://doi.org/10.1109/CISS.2012.6310860

Erunkulu, O. O., Zungeru, A. M., Thula, I. G., Lebekwe, C., & Mosalaosi, M. (2024, June). A comparative analysis of alpha-beta-gamma and close-in path loss models based on measured data for 5G mobile networks. *Results in Engineering*, *22*, 102328.

https://doi.org/10.1016/j.rineng.2024.102328

Feng, Z. (2025, March). Application and Development of Radar Sensors in Autonomous Driving Technology. *Applied and Computational Engineering*, *140*(1), 48–52. https://doi.org/10.54254/2755-2721/2025.21277

Fens, R. A. M., Ruggiano, M., & Leus, G. (2008). Channel Characterization Using Radar for Transmission of Communication Signals.

Fuschini, F., El-Sallabi, H., Degli-Esposti, V., Vuokko, L., Guiducci, D., & Vainikainen, P. (2008, March). Analysis of Multipath Propagation in Urban Environment Through Multidimensional Measurements and Advanced Ray Tracing Simulation. *IEEE Transactions on Antennas and Propagation*, *56*(3), 848–857. https://doi.org/10.1109/TAP.2008.916893

Gil, G.-T., Lee, J. Y., & Cho, D.-H. (2021). Estimation of Path Loss Parameters of a Sub-Terahertz Wireless Channel Using Monostatic Radar. *IEEE Access*, *9*, 52654–52663. https://doi.org/10.1109/ACCESS.2021.3070378

Guo, M., Sun, Z., Yang, S., & Fu, Y. (2017, November). Genetic algorithm improved spatial diversity 24-GHz FMCW radar with multipath for automotive applications. In *2017 Progress in Electromagnetics Research Symposium - Fall (PIERS - FALL)* (pp. 1988–1993). https://doi.org/10.1109/PIERS-FALL.2017.8293463

Gupta, S., Rai, P. K., Kumar, A., Yalavarthy, P. K., & Cenkeramaddi, L. R. (2021, September). Target Classification by mmWave FMCW Radars Using Machine Learning on Range-Angle Images. *IEEE Sensors Journal*, *21*(18), 19993–20001. https://doi.org/10.1109/JSEN.2021.3092583

Ha, K.-W., Lee, J.-Y., Kim, J.-G., & Baek, D. (2018, April). Design of Dual-Mode Local Oscillators Using CMOS Technology for Motion Detection Sensors. *Sensors*, *18*(4), 1057. https://doi.org/10.3390/s18041057

Holleman, I., Huuskonen, A., Kurri, M., & Beekhuis, H. (2010, January). Operational Monitoring of Weather Radar Receiving Chain Using the Sun. *Journal of Atmospheric and Oceanic Technology*, *27*(1), 159–166. (Publisher: American Meteorological Society) https://doi.org/10.1175/2009jtecha1213.1

Inggs, M., Griffiths, H., Fioranelli, F., Ritchie, M., & Woodbridge, K. (2014, October). Multistatic radar: System requirements and experimental valida-

tion. In *2014 International Radar Conference* (pp. 1–6). Lille, France: IEEE. https://doi.org/10.1109/RADAR.2014.7060435

Ji, B., Xue, B., Chen, P., & Wang, W. (2024, March). Analysis of Channel Characteristics for FMCW Millimeter-Wave Radar in Traffic Scenarios. In *2024 18th European Conference on Antennas and Propagation (EuCAP)* (pp. 1–4). https://doi.org/10.23919/EuCAP60739.2024.10501336

Jiang, H., Mukherjee, M., Zhou, J., & Lloret, J. (2021, January). Channel Modeling and Characteristics for 6G Wireless Communications. *IEEE Network*, *35*(1), 296–303. https://doi.org/10.1109/MNET.011.2000348

Kumari, P., Choi, J., Gonzalez-Prelcic, N., & Jr, R. W. H. (2017, February). *IEEE 802.11ad-based Radar: An Approach to Joint Vehicular Communication-Radar System*. arXiv. (arXiv:1702.05833 [cs]) https://doi.org/10.48550/arXiv.1702.05833

Lambot, S., Slob, E. C., Van Den Bosch, I., Stockbroeckx, B., Scheers, B., & Vanclooster, M. (2004, April). Estimating soil electric properties from monostatic ground-penetrating radar signal inversion in the frequency domain. *Water Resources Research*, *40*(4), 2003WR002095. https://doi.org/10.1029/2003WR002095

Li, X., He, J., Wang, C., Tang, S., & Hou, X. (2017, January). Evaluation of Surface Clutter for Future Geostationary Spaceborne Weather Radar. *Atmosphere*, *8*(1), 14. https://doi.org/10.3390/atmos8010014

Li, X., Wang, X., Yang, Q., & Fu, S. (2021). Signal Processing for TDM MIMO FMCW Millimeter-Wave Radar Sensors. *IEEE Access*, *9*, 167959–167971. (Conference Name: IEEE Access) https://doi.org/10.1109/ACCESS.2021.3137387

Liu, T., Guan, K., He, D., Takis Mathiopoulos, P., Wang, Y., Liu, F., & Ma, Y. (2024, November). A New Sensing Channel Modeling Approach Based on Ray Tracing and Stochastic Methods for Vehicle-to-Everything Applications. *IEEE Internet of Things Journal*, *11*(21), 34991–35006. (Conference Name: IEEE Internet of Things Journal) https://doi.org/10.1109/JIOT.2024.3436580

Morais, J., Behboodi, A., Pezeshki, H., & Alkhateeb, A. (2022, September). *Position Aided Beam Prediction in the Real World: How Useful GPS Locations Actually Are?* arXiv. (arXiv:2205.09054 [eess]) https://doi.org/10.48550/arXiv.2205.09054

Nguyen, P. T., Nhat, V. T., & Huynh, C. P. (2014, October). A high-resolution short-range

X-band FMCW radar system for ranging applications. In *2014 International Conference on Advanced Technologies for Communications (ATC 2014)* (pp. 675–680). Hanoi: IEEE. https://doi.org/10.1109/ATC.2014.7043473

Park, H., Kim, M., Jung, Y., & Lee, S. (2022, November). Method for Improving Range Resolution of Indoor FMCW Radar Systems Using DNN. *Sensors*, *22*(21), 8461. https://doi.org/10.3390/s22218461

Pralon, L., Pompeo, B., & Fortes, J. M. (2015, April). Stochastic analysis of random frequency modulated waveforms for noise radar systems. *IEEE Transactions on Aerospace and Electronic Systems*, *51*(2), 1447–1461. https://doi.org/10.1109/TAES.2014.140072

Prokopovich, I., Popov, A., Pajewski, L., & Marciniak, M. (2017, December). Application of Coupled-Wave Wentzel-Kramers-Brillouin Approximation to Ground Penetrating Radar. *Remote Sensing*, *10*(1), 22. https://doi.org/10.3390/rs10010022

Ramasubramanian, K. (2017, December). mmWave Radar for Automotive and Industrial Applications. Retrieved from https://www.ti.com/content/dam/videos/external-videos/en-us/2/3816841626001/5675916489001.mp4/subassets/Mmwave_webinar_Dec2017.pdf

Rameez, M., Pettersson, M. I., & Dahl, M. (2022, October). Interference Compression and Mitigation for Automotive FMCW Radar Systems. *IEEE Sensors Journal*, *22*(20), 19739–19749. (Publisher: Institute of Electrical and Electronics Engineers (IEEE)) https://doi.org/10.1109/jsen.2022.3204505

Rao, S. (2017, April). Introduction to mmwave Sensing: FMCW Radars. Retrieved from https://training.ti.com/sites/default/files/docs/mmwaveSensing-FMCWofflineviewing_2.pdf

Richards, M. A., Scheer, J. A., & Holm, W. A. (2010). *Principles of modern radar*. Raleigh (N.C.): SciTech publ.

Samad, M. A., Choi, S.-W., Kim, C.-S., & Choi, K. (2023). Wave Propagation Modeling Techniques in Tunnel Environments: A Survey. *IEEE Access*, *11*, 2199–2225. https://doi.org/10.1109/ACCESS.2022.3233877

Scannapieco, A., Renga, A., & Moccia, A. (2015, January). Preliminary Study of a Millimeter Wave FMCW InSAR for UAS Indoor Navigation. *Sensors*, *15*(2), 2309–2335.

https://doi.org/10.3390/s150202309

Scherr, S., Afroz, R., Ayhan, S., Thomas, S., Jaeschke, T., Marahrens, S., … Zwick, T. (2017, October). Influence of Radar Targets on the Accuracy of FMCW Radar Distance Measurements. *IEEE Transactions on Microwave Theory and Techniques*, *65*(10), 3640–3647. https://doi.org/10.1109/TMTT.2017.2741961

Sharifisoraki, Z., Amini, M., & Rajan, S. (2024, January). Comparative Analysis of mmWave Radar-based Object Detection in Autonomous Vehicles. In *2024 IEEE International Conference on Consumer Electronics (ICCE)* (pp. 1–6). (ISSN: 2158-4001) https://doi.org/10.1109/ICCE59016.2024.10444405

Sokol, Z., Szturc, J., Orellana-Alvear, J., Popová, J., Jurczyk, A., & Célleri, R. (2021, January). The Role of Weather Radar in Rainfall Estimation and Its Application in Meteorological and Hydrological Modelling—A Review. *Remote Sensing*, *13*(3), 351. (Publisher: MDPI AG) https://doi.org/10.3390/rs13030351

Son, Y.-S., Sung, H.-K., & Heo, S. W. (2018, August). Automotive Frequency Modulated Continuous Wave Radar Interference Reduction Using Per-Vehicle Chirp Sequences. *Sensors*, *18*(9), 2831. https://doi.org/10.3390/s18092831

Soumya, A., Krishna Mohan, C., & Cenkeramaddi, L. R. (2023, January). Recent Advances in mmWave-Radar-Based Sensing, Its Applications, and Machine Learning Techniques: A Review. *Sensors*, *23*(21), 8901. (Number: 21 Publisher: Multidisciplinary Digital Publishing Institute) https://doi.org/10.3390/s23218901

Sun, S., Rappaport, T. S., Rangan, S., Thomas, T. A., Ghosh, A., Kovacs, I. Z., … Jarvelainen, J. (2016, May). Propagation Path Loss Models for 5G Urban Micro- and Macro-Cellular Scenarios. In *2016 IEEE 83rd Vehicular Technology Conference (VTC Spring)* (pp. 1–6). https://doi.org/10.1109/VTCSpring.2016.7504435

Texas Instruments. (2018). *Raw adc data to dbfs* (Tech. Rep.). (Application note on FFT scaling and power measurement from ADC output) Retrieved from [2025-05-08]https://e2e.ti.com/cfs-file/__key/communityserver-discussions-components-files/1023/0647.Raw-ADC-data-to-dBFs.pdf

Texas Instruments. (2024, February). *Awr2243 single-chip 76- to 81-ghz fmcw transceiver datasheet* (Tech. Rep. No. SWRS223D). Texas Instruments. (Datasheet for the AWR2243 FMCW Transceiver) Retrieved from [2025-05-08]https://www.ti.com/

lit/gpn/AWR2243

Wan, R., Song, Y., Mu, T., & Wang, Z. (2019, July). Moving Target Detection Using the 2D-FFT Algorithm for Automotive FMCW Radars. In *2019 International Conference on Communications, Information System and Computer Engineering (CISCE)* (pp. 239–243). Haikou, China: IEEE. https://doi.org/10.1109/CISCE.2019.00062

Wang, H.-N., Huang, Y.-W., & Chung, S.-J. (2017, February). Spatial Diversity 24-GHz FMCW Radar With Ground Effect Compensation for Automotive Applications. *IEEE Transactions on Vehicular Technology*, *66*(2), 965–973. (Conference Name: IEEE Transactions on Vehicular Technology) https://doi.org/10.1109/TVT.2016.2565608

Wang, X., He, D., Guan, K., Duan, H., Dou, J., AbuAli, N. A., & Zhong, Z. (2024, March). Channel Measurement and Modeling for Millimeter-Wave Automotive Radar. *IEEE Transactions on Intelligent Transportation Systems*, *25*(3), 2933–2943. (Conference Name: IEEE Transactions on Intelligent Transportation Systems) https://doi.org/10.1109/TITS.2023.3285948

Wang, Z., Li, S., Liu, Y., & Wang, S. (2024, May). Analysis and Optimization of FI Path Loss Model in 39GHz Indoor Line-of-Sight Scenario Based on MMSE. In *2024 International Conference on Microwave and Millimeter Wave Technology (ICMMT)* (Vol. 1, pp. 01–03). (ISSN: 2994-3124) https://doi.org/10.1109/ICMMT61774.2024.10671627

Wei, Z., Jia, J., Niu, Y., Wang, L., Wu, H., Yang, H., & Feng, Z. (2024). Integrated Sensing and Communication Channel Modeling: A Survey. *IEEE Internet of Things Journal*, 1–1. (Conference Name: IEEE Internet of Things Journal) https://doi.org/10.1109/JIOT.2024.3449377

Xiongwen Zhao, & Vainikainen, P. (2001, August). Multipath propagation study combining terrain diffraction and reflection. *IEEE Transactions on Antennas and Propagation*, *49*(8), 1204–1209. https://doi.org/10.1109/8.943315

Zhang, G., Li, H., & Wenger, F. (2020, May). Object Detection and 3d Estimation Via an FMCW Radar Using a Fully Convolutional Network. In *ICASSP 2020 - 2020 IEEE International Conference on Acoustics, Speech and Signal Processing (ICASSP)* (pp. 4487–4491). Barcelona, Spain: IEEE. https://doi.org/10.1109/ICASSP40776.2020.9054511